Chronology of sedimentation and landscape evolution in the Okavango Rift Zone, a developing young rift in southern Africa

S. Vainer[1,2]*, C. Schmidt[1], E. Garzanti[3], Y. Ben Dor[4], G. Pastore[3], T. Mokatse[1], C. Prud'homme[1,5], L. Leanni[6], G. King[1], ASTER Team[6]†, E. P. Verrecchia[1,7]

[1]Institute of Earth Surface Dynamics, University of Lausanne, 1015 Lausanne, Switzerland. [2]GET (Université de Toulouse, CNRS, IRD, UPS, CNES), 31400 Toulouse, France. [3]Department of Earth and Environmental Sciences, University of Milano-Bicocca, 20126 Milano, Italy. [4]Geological Survey of Israel, 32 Yesha'yahu Leibowitz, Jerusalem 9692100, Israel. [5]Centre de Recherches Pétrographiques et Géochimiques, Université de Lorraine, CNRS, 54500 Vandœuvre-lès-Nancy, France. [6]Aix-Marseille Université, CNRS, Collège de France, IRD, INRA, CEREGE, 13545 Aix-en-Provence, France. [7]Earth and Environmental Sciences, Botswana International University of Science and Technology, Palapye, Botswana

*Corresponding author: Shlomy Vainer (shlomy.vainer@mail.huji.ac.i)

† Group separate identification: Georges Aumaître, Didier L. Bourlès & Karim Keddadouche

Key Points:

- Nascent continental rifting stages are reflected through sedimentological variations
- Eolian sand that was formed before alluvial incision into the rift is preserved on elevated surfaces
- Depositional environments in the incised rift have shifted into alluvial-lacustrine conditions around the Middle Pleistocene Transition

Abstract

The Kalahari Basin in southern Africa, shaped by subsidence and epeirogeny, features the Okavango Rift Zone (ORZ) as a significant structural element characterized by diffused extensional deformation forming a prominent depocenter. This study elucidates the Pleistocene landscape evolution of the ORZ by examining the chronology of sediment formation and filling this incipient rift and its surroundings.

Modeling of cosmogenic nuclide concentrations in surficial eolian sand from distinct structural blocks around the ORZ provides insights into sand's residence time on the surface. Sand formation occurred from ~2.2 to 1.1 Ma, coinciding with regional tectonic events. Notably, provenance analyses of sand within ORZ's lowermost block where large alluvial fans are found indicate different source rocks and depositional environments than those of the eolian sands found at a higher elevation. This suggests that the major phase of rift subsidence and the following incision of alluvial systems into the rift occurred after eolian dune formation. Luminescence dating reveals that deposition in alluvial fan settings in the incised landscape began not later than ~250 ka, and that a lacustrine environment existed since at least ~140 ka.

The established chronological framework constrains the geomorphological effects of the different tectono-climatic forces that shaped this nascent rifting area. It highlights two pronounced stages of landscape development, with the most recent major deformation event in

the evolving rift probably occurring during the middle Pleistocene transition (1.2-0.75 Ma). This event is reflected as a striking change in the depositional environments due to the configurational changes accompanying rift progression.

Plain Language Summary

Early stages of continental rifting in the Okavango Rift Zone are described from the perspective of sediment dynamics by constructing a time frame for their evolution. Two major types of sediment and their corresponding time scales are studied. The older sediments are eolian sands that were formed between ~2.2 and 1.1 million years ago, lying today on elevated structural surfaces above the incised rift. Within the subsiding rift that was significantly geomorphologically modified not earlier than 1 million years ago, sediments were deposited by alluvial fans at least since 250 thousand years ago, and were followed by a lacustrine environment with alternating hydrological conditions, since at least 140 thousand years ago.

1. Introduction

Tectonic geomorphology incorporates various disciplines and is an evolving field with recent advances in geochronological methods (Keller and DeVecchio 2013; Owen, 2022). While numeric age determinations are being widely used to reconstruct and quantify landscape evolution, multiple processes are involved in the buildup of the analyzed proxies such that their interpretation must be consistent with the geomorphologic context (Watchman and Twidale, 2002; Le Dortz et al., 2012; Brown, 2020). Among the most studied features for elucidating and evaluating the effects of tectonics and climate on landscape evolution are alluvial and fluvial subaerial fans, which are common also in rift settings and experience a highly dynamic geomorphological history (Gierlowski-Kordesch, 2010; Warren; 2010; Scheinert et al., 2012; Bowman, 2019).

Subaerial fans are generally found and best preserved at the base of mountain fronts within tectonically active zones, where changes in base level are induced by tectonics and variations in climate (Harvey, 2002; Blair and McPherson, 2009). Extensive research has been performed to study their morphologies, involved processes and mechanisms, as well as the components within the system (e.g., nature of sediments, vegetation, lithology) and to reconcile the respective roles of climate and tectonics in their formation (Lustig, 1965; Hooke, 1967; Ritter et al., 1995; Viseras et al., 2003; Terrizzano et al., 2017; Harvey et al., 2018; Bowman, 2019). Multiple models for the environmental evolution of fans were formulated based on disparate methods and over a biased global spatial distribution and settings as most of the primary studies were conducted in the American southwest (Lecce, 1990; Scheinert et al., 2012; Stock, 2013).

The Okavango Rift Zone (ORZ; Figure 1), in interior southern Africa, constitutes an intriguing area to study tectonic geomorphology through the stages involved in the development of alluvial fans and lacustrine/palustrine environments during nascent rifting (Scholz et al., 1976; Kinabo et al., 2007; Wright et al., 2021; Paulssen et al., 2022), where globally unique megafans and paleo-lakes are preserved (Shaw and Thomas, 1992; Burrough and Thomas, 2013). Paleo-lacustrine environments have been thoroughly studied in this area (Moore et al., 2012 and references therein) but, apart from the numerous studies of the Okavango Delta (Podgorski et al., 2013; McCarthy, 2013 and references therein), little attention has been given to the early evolution of fans in central southern Africa (Blair and McPherson, 2009; Wilkinson et al., 2023). Moreover,

as the ORZ is bordered by eolian dunes and was subjected to varying zonal climatic interactions (Partridge, 1993; Shaw and Thomas, 1988; Burrough and Thomas, 2013), chronological constraints of landscape evolution that precede the most recent eolian deposition stages are rare (Moore et al., 2012; McCarthy, 2013; Vainer et al., 2021). Therefore, as favored in other regions and settings where recent and earlier fans were studied and compared (DeCelles and Cavazza, 1999; Harvey et al., 2005), an investigation of previous phases of landscape development along the ORZ is required.

The ORZ lies within the largest continuous sand sheet on Earth and preserves remnants of vast waterbodies (Figure 2a) (Grove, 1969; Baillieul 1975; Burrough and Thomas, 2013; McCarthy, 2013; Wilkinson et al., 2023). The largest active fan within the ORZ, (i.e. Okavango Delta), is characterized by the lowest slope gradient of any other studied subaerial fan and defines one out of three end members of fan types, representing the “losimean” character which is governed by anastomosing meanders (Stanistreet and McCarthy 1993; Bowman, 2019; Wright et al., 2021). Although the Okavango Delta is one of the largest alluvial fans in Africa (McCarthy, 1993) and comprises today the most active depocenter in the Kalahari Basin (Figure 1), isopach maps reveal that, the main depocenter in the Okavango Basin lies ~100 km to the northeast of the Okavango Delta (Figure 2a). This area occupies the Linyanti-Chobe Basin within the Chobe Enclave (CE) (together with the Zambezi Fan this region is also referred to as the Mid-Zambezi Rift) (Figure 2), which hosts a large alluvial fan that is partially truncated due to tectonic activity (Shaw and Thomas, 1992; McCarthy, 2013; Mokatse et al., 2022a; Wilkinson et al., 2023).

While chronological studies of alluvial fans' evolution have shed light on the relationships between their development and tectonics (e.g. Matmon et al., 2006; Placzek et al., 2010; Porat et al., 2010; Terrizzano et al., 2017), the affinity between tectonic settings and eolian accumulation and preservation is poorly constrained and largely unquantified (Cosgrove et al., 2022). Furthermore, it has been postulated that not all fan surfaces are suitable to be dated, particularly at sites where signs of weathering, reworking, and changes in sources are evident (Watchman and Twidale, 2002; Matmon et al., 2005). Due to the prevalence of these processes in the CE, being a tectonically active sector of the ORZ (Garzanti et al., 2022; Gaudaré et al., 2024), and the uncertainties of available chronological constraints (Moore et al., 2012; McCarthy, 2013), an adjustment of conventional dating methods is needed to construct a chronological framework of this terrane.

This study constructs a temporal framework of the geomorphological response to the incipient rifting stages of the ORZ, the southwestern most part of the East African Rift System (EARS). Along the related segments of this rifting system, the latest age constraints for down-warping and faulting are of Pliocene age Michon et al., 2022) (Figure 1). Therefore, rift-related deformation in the ORZ is expected to occur from the Pliocene onwards. Following this assumption, we apply luminescence-based chronologies of buried deposits of the Cuando Megafan, lying in the heart of the ORZ (i.e., CE), with cosmogenic nuclide-based residence time estimates of the surrounding regional eolian sand (Figure 2). These chronometers cover together three relevant temporal orders of magnitude (10^4-10^6 yr), providing a time frame for the fluvial-palustrine-lacustrine sediment accumulation in the CE and for sand supply into the central Kalahari. Mineralogical and textural inspections of the sediment are used to characterize the depositional environments and sediment sources. Finally, the data are combined to form a conceptual model of landscape evolution during the early stages of continental rifting.

Figure 1. Structural elements in southern Africa including the main East African Rift Fault System (Chorowicz, 2005), areas where rifting is chronologically constrained (Michon et al., 2022), intracratonic structural axes that have been operated since the Neogene (Haddon and McCarthy, 2005), and the Okavango Rift Zone Fault System (Modisi et al., 2000; Kinabo et al., 2008; Bäumle et al., 2019). The background is an 90 m hill-shaded DEM (Farr et al., 2007). Inset denotes the extent of the map on the African continent with its political boundaries.

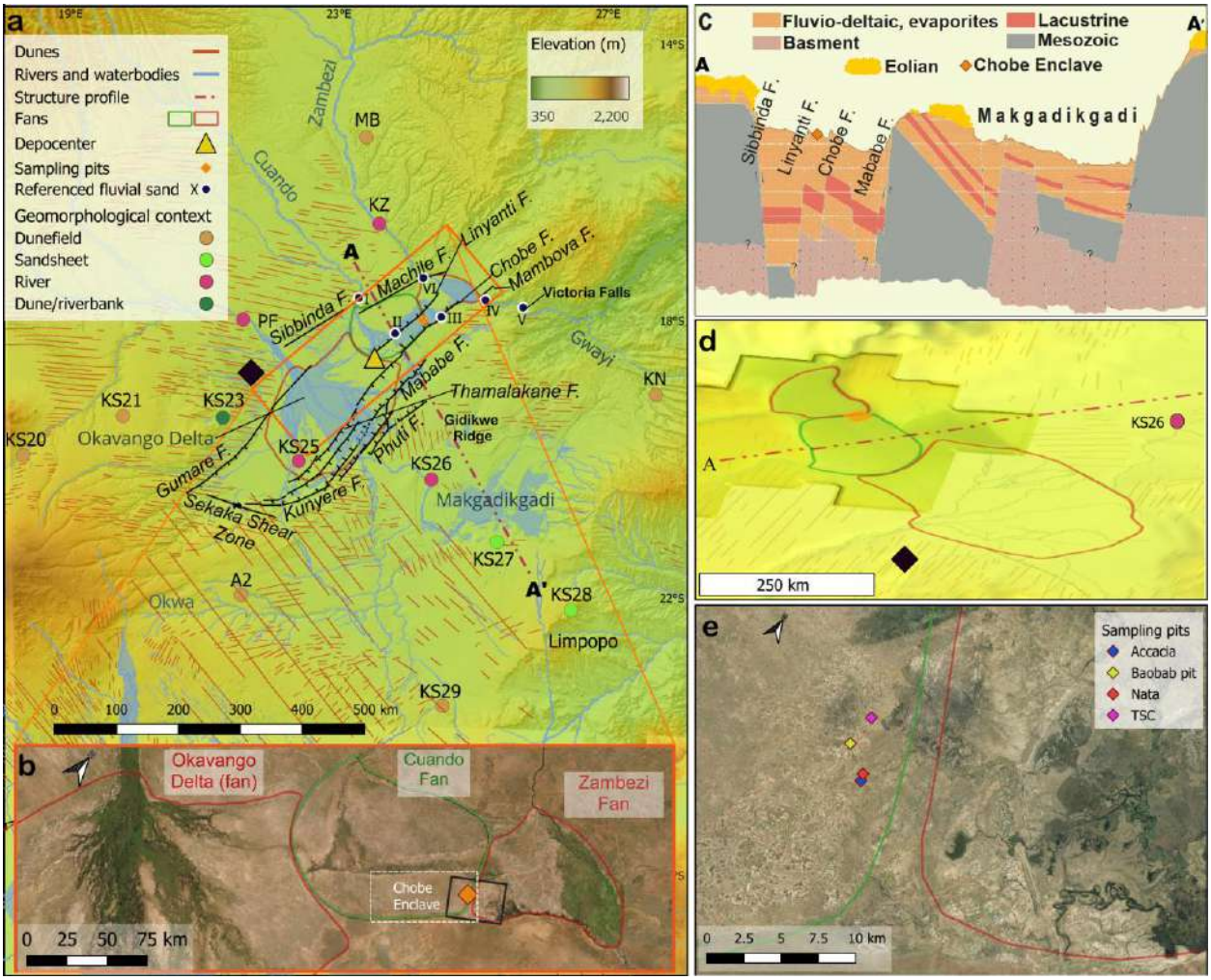

Figure 2. (a) Geomorphology of the Makgadikgadi–Okavango–Zambezi Basin including sand dunes (Thomas and Shaw, 1991), faults (Modisi et al., 2000; Kinabo et al., 2008; Bäumle et al., 2019), hydrogeological features (OpenStreetMap.org; MapCruzin.com), and the alluvial fans of the Okavango Rift Zone (Wilkinson, 2023). The background is a 30 m hill-shaded DEM (Farr et al., 2007) (b) Satellite image of the northeastern ORZ (ESRI, 2023) depicting the Linyanti-Chobe Basin and its peripherical alluvial fans. (c) Surface topography (vertical exaggeration ≈ 500) and conceptual geological cross-section (not to scale) through the Makgadikgadi–Okavango–Zambezi Basin (after Bäumle et al., 2019). The horizontal axis corresponds to the semi-dashed line in a. (d) 3D elevation model of the ORZ constructed from 12.5-m DEM of PALSAR's L-band SAR and its margins modeled from 30 m DEM (ALOS PALSAR, 2010). Black diamond is located at the same place as in *a* to ease orientation. (e). Locations of sampling pits in the Chobe Enclave superimposed on a satellite image (ESRI, 2023).

2. Regional background

2.1. Structural Geology

The ORZ is defined by eleven recognized major fault systems (Kinabo et al., 2008) that are situated between the Congo and Kalahari cratons, overlying extensional and accretional structures of Proterozoic and Mesozoic age (Dixey, 1956; Doucouré and de Wit, 2003; Oriolo and Becker, 2018) and is considered the southwestern-most segment of EARS (Fairhead and Girdler, 1969; Reeves, 1972; Daly et al., 2020) (Figure 1). The EARS comprises two main branches, the more evolved eastern branch which has been active since the Oligocene, and the younger western branch with main activity since the lower Miocene (Michon et al., 2022). While both branches include individual rift basins that are linked by transfer zones, a network of separate rift basins extends from the west of Lake Tanganyika in the northeast to the Okavango in the southwest (Figure 1). This southwestern branch displays geophysical attributes of the main EARS and was formed during the Quaternary ensuing a major late Pliocene phase of regional deformation (Partridge and Maud, 1987; Vainer et al., 2021).

The 400 km long and 150 km wide structural trough of the ORZ is bounded by elevated structural arches forming a syntectonic depocenter (Gumbricht et al., 2001) (Figures 1, 2). It is controlled by NE-SW normal to dextral strike-slip faults forming half-graben structures (; Modisi et al., 2000; Kinabo et al., 2007; Kinabo et al., 2008) that accommodate an endorheic hydrological system where the main river channels are fault controlled (Modisi, 2000) (Figure 2). Several tectonic mechanisms were attributed to the sagging of the ORZ including extension resulting from the advancement of the EARS (Modisi et al., 2000; Wright, 2021) inter-cratonic strains causing lithospheric stretching (Pastier et al., 2017; Yu et al., 2017), as well as Internal and peripheral epeirogenic deformation of the Kalahari Basin (Moore, 1999; Vainer et al., 2021).

Structure and hydrology suggest links between the ORZ and the Makgadikgadi Basin (Figure 2). In the Makgadikgadi Basin, a “staircase” topography is suggested to be fault-controlled in places with a maximum vertical throw of over 10 m, but the structures and kinematics imply that this basin is not an EARS-related tectonic depression (Eckardt et al., 2016; Gaudaré et al., 2024). Furthermore, while ongoing tectonic activity in the Linyanti-Chobe (Zambezi) and Okavango basins is widely accepted (Dumisani, 2001; Daly et al., 2020), signs of recent tectonic imprint on the landscape in the Makgadikgadi Basin are low to absent. In a broad morpho-structural study, Gaudaré et al. (2024) conclude that the evolving kinematic propagation of the rift-related fault system left the Makgadikgadi Basin tectonically inactive at least since the early Holocene, with recent deformation localized in the ORZ.

The CE (17.94° 18.36°S, 23.93° 24.59°E) lies between two faults in the heart of the ORZ, where movements along these faults caused substantial changes in the landscape diversion of the hydrological system changing the courses of the Cuando and Zambezi rivers (Mallick et al., 1981; Moore and Larkin, 2001). The latest geomorphic response to faulting in the CE was dated to ~ 6 ka (Mokatse et al., 2022b), and ongoing high seismicity is recorded (Dumisani, 2001). According to the model proposed by Gaudaré et al. (2024) for the nature of deformation in the ORZ, the CE constitutes a transfer zone between the active segments, accommodating variations in the deformation between diverging plates. The CE is controlled by the active Chobe Fault to the south ranging in length from 150 to 250 km while displaying ~40 m scarp height, and the

active Linyanti Fault of 75-150 m in length and ~8 m scarp height. These faults are in different temporal stages of evolution, recording older phases of linkage with fault segments. Today, with the progression of the rift basin, they are bending toward each other to overlap without merging (Kinabo et al., 2008), expected to activate future deformation leading to the capturing of the Okavango System by the Linyanti-Zambezi System (McCarthy et al., 2002). This places the CE as a dynamic terrane that is expected to record ancient and recent stages of deformation and rift propagation (Mokatse et al., 2022a).

2.2. Chronostratigraphy

Cenozoic fluvio-lacustrine and eolian sediments (Kalahari Group) up to 300 m-thick fill the MOZB (Haddon and McCarthy, 2005; Podgorski et al., 2013) that was established to form a similar configuration as today around 2.5 Ma (Du Toit, 1933; Day et al., 2009; Cotterill & De Wit, 2011; Vainer et al., 2021). However, a differential structural geometry probably already existed during the Pliocene (Vainer et al., 2021) comprising three sub-basins at the sub-surface, with the thickest depocenter located between the Okavango and Linyanti-Chobe (Haddon and McCarthy, 2005). Basement rocks, mostly Proterozoic volcanic and metasedimentary rocks, as well as Mesozoic metasediments of the Karoo Supergroup and Lower Jurassic basalts are rarely exposed in marginal and deformed areas within the MOZB. Substantial portions of basement rocks in the ORZ are covered by post-Karoo basalts and more recent dolerite dykes, forming a 60 km wide, west- northwest-east-southeast trending swarm with average dyke spacing of ~2.3 km (Modisi, 2000). The lithology and composition of the Kalahari Group within the MOZB are known from limited boreholes mainly drilled in the Okavango sub-basin. They reveal the prevalence of sand derived from both local and distant, mostly northerly, source areas, with variable proportions of silt, clay, and carbonates that underwent in places a high degree of chemical weathering (Huntsman-Mapila et al., 2005; Vainer et al., 2021).

Deposition in the ORZ is characterized by sediments that were transported into the basin, and then recycled, weathered, and eventually diagenetically altered or cemented by secondary minerals (Huntsman-Mapila et al., 2005; Vainer et al., 2021; Garzanti et al., 2022; Mokatse et al., 2023). A major change in the organization of fluvial systems is assumed to have occurred in the early Pleistocene when the upper part of the Zambezi River was captured by its middle part, diverting flow from the terminal basin into the lower base level of the Indian Ocean (Moore et al., 2012; Vainer et al., 2021). Today, the Okavango Basin is occupied by divide fans that are characterized by hydrological links with neighboring basins (Wilkinson et al., 2023). Within the Okavango Basin, a series of tectonically generated reorganizations of the fluvio-lacustrine system occurred throughout the Quaternary (Moore et al., 2007, Schmidt et al., 2023). These events resulted in the deposition of mixed alluvial, fluvial, palustrine, and evaporite sediments, surrounded by eolian deposits on the elevated basin margins.

The only numeric ages for the earliest deposition in the MOZB are derived from cosmogenic nuclide-based burial dating of two depth profiles in the western Okavango Basin. Ages are 3.06 $^{+4.4}/_{-0.46}$ Ma at the base of the upthrown block and 3.35 $^{+0.39}/_{-0.26}$ Ma in the downthrown block, where basal strata were undatable. The uppermost consolidated sediments at these upthrown and downthrown sites were buried at $1.12^{+0.13}/_{-0.12}$ and 1.34 $^{+0.16}/_{-0.14}$ Ma, respectively. These capping ages were suggested to represent the onset of eolian dominance for sand transport and deposition (Vainer et al., 2021).

The surficial fluvio-lacustrine features of the MOZB represent several depositional phases, resulting from changes in fluvial configuration and deposition on top of older alluvium (Thomas and Shaw, 1991). Various materials collected mostly from ridges and pan floors were dated by applying luminescence and ^{14}C dating techniques and were interpreted to represent alternating wet and dry stages (Burrough et al., 2007; Burrough and Thomas, 2013). Earliest ages, as old as 280 ka, were evoked from a limited number of samples (n=3) in these studies, leaving a noticeable age gap with the ~1.1 Ma burial ages at the western MOZB. Successive lacustrine highstands were inferred to occur between 131 ± 11 and 92 ± 2 ka, with another phase centered around 64 ka, and fluctuating conditions between 40 ka and the present. The period between 115 and 95 ka coincides with eolian accumulation in dunes at the northeastern MOZB (Stokes et al., 1998) and the younger inferred highstand stages are coeval with dune buildup in northwestern MOZB areas (Thomas et al., 2000). Within the CE, ages of depth profiles in elevated ridges range between 23.4 ± 1.6 and 1.9 ± 0.3 ka (Burrough and Thomas, 2008; Mokatse et al., 2022), while quartz in carbonate rocks was dated at 48.2 ± 9.6 ka and buried floodplain sands to ~50 ka (Diaz et al., 2019). Combined, these ages indicate a dynamic hydrogeological fluvio-lacustrine environment at least since ~280 Ka.

3. **Sampling, sample preparation, and analyses**

3.1 Site selection and sedimentological characterization

Four pits were excavated to depths of 8-10 m between the Chobe and Linyanti faults within the Cuando alluvial fan, as part of an interdisciplinary framework focusing on the significance of terrestrial carbonate deposits. Hence, the locations of the pits were chosen based on several considerations including their current geomorphological context, structural context along the faulting transfer zone, and accessibility. The multidisciplinary research of the same sediment samples allows an extensive interpretation of various proxies including additional mineralogical data and paleoenvironmental interpretation published by Mokatse et al. (2023) and is referenced below.

The compromised localities of sites from north to south are termed TSC, BP, Nata, and Acacia covering an area of ~5 km^2 (Figure 2e). Sampling was made in regular intervals of 0.4 m where available, and particularly higher resolution where adjacent facies changes were visible at the field. Field inspection of the sediment was accompanied by grain size distribution analyses of all samples (n=54) to classify sedimentary facies and identify shifts in depositional environments. These analyses were performed by using a laser diffraction Beckmann Coulter LS 13320 on the <2 mm size fraction of carbonate and organic matter-free material.

3.2 Optically stimulated luminescence (OSL) dating

Each stratigraphical unit containing an ample amount of quartz was sampled for OSL dating. Sampling was made via light-sealed tubes hammered into pit walls or by auger downwards from the bottom of the pit for the deepest samples. Additionally, 1-3 surficial quartz-containing carbonate samples from each site were sampled to constrain the timing of diagenetic processes

(i.e. carbonate cementation). These carbonate samples were then cut under subdued red lighting to remove any material that was exposed to light and the remaining inner, un-exposed parts were further treated for analyses.

Organic matter and carbonate precipitates were removed from the 180-212 µm size fraction of all samples with H_2O_2 and 10% HCl, respectively. Using dense-liquid (sodium polytungstate) separation, the fraction between 2.62 and 2.70 g cm^{-3} was etched for 40 min with 40% HF acid to purify the quartz separates and remove the outer layer affected by alpha-radiation. Subsequently, the samples were treated with 10% HCl for >1 h for dissolution of potential Ca-fluoride precipitates (Diza et al., 2016).

The equivalent dose (D_e) of quartz samples was determined using a single-aliquot regeneration dose (SAR) protocol, including four regeneration doses, a zero dose, and a repeated dose (Murray and Wintle, 2000). Preheat plateau and dose recovery tests were carried out in the temperature range of 180–260 °C for three samples from different profiles to identify optimal preheat conditions. Dose response data constructed from the first 0.7 s of the decay curve (corrected for a background estimated from the last 2 s of this curve) were fitted with an exponential plus linear function in the Analyst software (v4.57; Duller, 2015). Further technical details are given in the Supporting Information. Radioelement concentrations (K, Th, U) were quantified by high-resolution γ-ray spectrometry on ground samples with a mass of ~60–80 g that were stored in a sealed container for at least four weeks prior to analysis.

3.3. Cosmogenic nuclides

Thirteen surficial sand samples from river sands and eolian dunes were processed to determine their ^{10}Be and ^{26}Al content. Seven samples were collected from within the MOZB, and six from its periphery (Figure 2a). The sand was sieved, and the 250-850 µm size fraction underwent sample leaching by aqua regia solution, magnetic separation, and sequential HF + HNO_3 etching (Kohl and Nishiizumi, 1992). Major elements were measured with inductively coupled plasma optical emission spectrometry to verify low concentrations of elements such as Al or Ti. Following spiking and ion-exchange chromatography, isotopic ratios of oxidized targets were measured by accelerator mass spectrometry at Centre de Recherche et d'Enseignement des Géosciences de l'Environnement (CEREGE), France. Isotopic ratios of the in-house standards used for measurements were $7.40*10^{-12}$ and $1.91*10^{-11}$ for $^{26}Al/^{27}Al$ and $^{10}Be/^{9}Be$, respectively. Procedural blank values were in the range between $8.6*10^{-16}$ and $1.66*10^{-15}$ for $^{26}Al/^{27}Al$ and between $2.68*10^{-16}$ and $6.97*10^{-15}$ for $^{10}Be/^{9}Be$.

3.4. Heavy minerals

Two samples from the base of each pit were analyzed for their heavy-mineral assemblage to detect the relative sediment contribution from the Cuando and Zambezi rivers. Heavy minerals were separated by centrifuging in sodium polytungstate (density ~2.90 g cm^{-3}) and recovered by partial freezing with liquid nitrogen. More than 200 transparent heavy-mineral grains were point-counted on grain mounts at suitable regular spacing under the petrographic microscope to minimize the bias caused by grain counting (Garzanti and Andò, 2019). Grains of uncertain identification were checked with Raman spectroscopy (Andò and Garzanti, 2014). Based on the percentage of transparent heavy minerals (tHM), tHM suites are defined as "extremely poor"

(tHMC < 0.1) and "very poor" (tHMC 0.1-0.5; Garzanti and Andò, 2007). The ZTR index is the sum of zircon, tourmaline, and rutile over total tHM (Hubert, 1962) and is classically used to estimate sediment "durability" (i.e., the extent of recycling; Garzanti, 2017).

4. Modelling

4.1. OSL dating

Due to the low radioactivity of the sand (Supporting information, Table S1), the cosmic dose rate makes up a significant contribution to the total dose rate (~25–65%, depending on the sample). Therefore, an assessment of the time-dependent cosmic dose rate has been made (Supporting Information, Figure S1). This has been estimated step by step by first accounting for the youngest samples taken from the carbonate unit, and hereafter calculating the cosmic dose rates of the samples taken from the sand unit below the carbonate layers, considering the age of the younger samples. Also, carbonate precipitation that can influence the dose rate calculation was considered (Supporting information, Table S2).

Two models were considered for carbonate units (Supporting information, Table S2). One assumes a short time between sand accumulation, carbonate precipitation, and pore filling, thus no modelling of carbonate emplacement over time and its influence on dose rate evolution is carried out (cf. Nathan and Mauz, 2008; Mauz and Hoffmann, 2014; Kreutzer et al., 2019). In case this assumption does not apply, the alternative approach was to perform sensitivity tests by contrasting the conventional OSL ages with those resulting from modelling the time-dependent dose rate using the RCarb model (Mauz and Hoffmann, 2014; Kreutzer et al., 2019). Also, the possibility of U uptake during carbonate precipitation was considered, but given that ^{226}Ra and daughter nuclides contribute >70% of the total β- and γ-dose rate it was concluded that modelling the time-dependent dose rate with reference to poorly constrained assumptions would probably not result in substantially changed ages, necessitating a revision of the environmental interpretation (Degering and Degering, 2020).

The age information obtained for the samples from the carbonate units was considered for estimating the cosmic dose rate applicable to the samples extracted from the sand units below. This approach of individually modelling the cosmic dose rate for each sample based on age information from stratigraphically younger samples was contrasted with the simple (and more common) approach of assuming a constant sedimentation rate (Supporting information, Table S3). This comparison reveals that the age estimates in both ways are indistinguishable at the 1σ confidence level. Therefore, the ages derived from a constant sedimentation rate are used as the TSC profile shows an almost linear increase in age with depth and because adopting one criterion consistently across the entire profile is simpler and more straightforward whenever age inversions occur.

Another factor causing potential OSL age inaccuracy is the internal dose rate of quartz grains. Especially in low-dose-rate environments, such as the CE, the contribution from the internal dose rate to the total dose rate can be significant. There are only a few previous studies on measured values of internal radioelement concentrations of quartz, and these yielded variable results (e.g.,

Vandenberghe et al., 2008; Steup, 2015). As the U and Th content of quartz seems to scatter to a much larger extent than, e.g., the K content of K-feldspar, it may not seem reasonable to assume a universal value for the internal quartz dose rate. Within the scope of this study, it was not possible to quantify the internal dose rate of the samples. A previous publication including OSL ages of comparable samples from the Okavango Basin does not report analytical values for the internal quartz dose rate but states that this dose rate contribution does not change the interpretation of the results (Burrough et al., 2009). Thus, zero internal quartz dose rate was assumed, with the implication that age estimates might be younger, should there be a significantly large internal dose rate from quartz grains.

The D_e used to estimate the burial age was derived from applying the Central Age Model (CAM; Galbraith et al., 1999), although some De distributions are slightly positively skewed (ln D_e between -0.5 and 0.9; see Supporting Information). Following previous studies in this area (Burrough et al., 2009), the CAM age model is applied as the overdispersion of a D_e dataset (Table 1) does not necessarily inform on the level of complete bleaching prior to burial (Guérin et al., 2015) and as this model also accommodates external beta dose rate heterogeneities more accurately than minimum age models. Ages were calculated with the DRAC software (v1.2; Durcan et al., 2015).

4.2. Surficial residence time

The surficial residence time of the sand was assessed through numerical modelling simulating the accumulation of cosmogenic nuclides under eolian, fluvial, or lacustrine settings by applying the Cosmolian model (Vainer et al., 2018a; Vainer and Ben Dor, 2021; Vainer et al., 2022). Simulations commence with the build-up of cosmogenic nuclides during erosion of source areas that are represented by the coordinates of the headwater of the sample specific-sub basin (Table S4, Supporting Information). Values of 3, 9, and 20 m Ma^{-1} were considered, following Regard et al. (2016) and references therein for erosion rates in the source areas of the sand (Garzanti et al., 2022). Simulations then reproduce the vertical component of sand grains during transport by randomly changing the overburden by 20 cm increments, with twenty-four combinations of possibilities of boundary conditions. The average latitude and altitude values of each sub-basin of a sample define the parameters for cosmogenic nuclides' production rates during transport and are changing only as a function of changing depth. Three amplitudes of 1, 10, and 25 m are used as different boundary conditions to encompass the range of dune heights (Lancaster, 1981; Stokes et al., 1998), and shallow waterbodies in the MOZB (Moore et al., 2012). The retention time at each depth increment is based on a probability function, constructed from dated eolian (Lancaster et al., 2016 and references therein), lacustrine (Huntsman-Mapila et al., 2006; Burrough and Thomas, 2008; Burrough and Thomas, 2013), fluvial (Shaw et al., 1992; Brook et al., 2008), and pluvial (Nash et al., 1981) sediments. Two datasets were constructed to form two probability functions by dividing the OSL/TL/^{14}C ages of buried sediments with the corresponding depth of each dated sample. This conversion from age to vertical displacement rates was applied to 54 eolian samples and 35 fluvial, lacustrine, and palustrine (FLP) samples. These two datasets were further modified to account for the possible bias stemming from oversampling shallow deposits by removing the fastest 10% from each dataset.

Each simulation during which the build-up of cosmogenic nuclides occurred lasted for 5 My and was repeated with the same conditions 10,000 times. The duration of various successful

simulations in which convergence between the simulated and measured concentrations of both ^{26}Al and ^{10}Be occurred have been summarized and are interpreted as the most probable timing since the modelled sand was introduced into the landscape (Vainer et al., 2022).

5. Results

5.1 OSL dating

Preheat and dose recovery tests informed on the most suitable preheat and cutheat temperatures (200 °C in our case, for 10 s and 0 s, respectively). The results of De estimation for a minimum of 39 aliquots per sample are shown in Table S1 in Supporting Information and calculated ages are listed in Table 1 and illustrated in Figure 3. . The assumption that the ^{238}U decay chain is in secular equilibrium was followed for samples that were taken from carbonate-cemented units. Ages of 29 ± 3 ka and 81 ± 7 ka for samples TSC 0.8 and TSC 2.0 were obtained, respectively. Samples NATA 0.8 and NATA 0.8B, taken from the same depth of 0.8 m, yielded ages of 74 ± 7 ka and 58 ± 6 ka, respectively, not overlapping at the 1σ confidence level. A sample taken 1.2 m below (NATA 2.0), however, produced an age of 64 ± 6 ka, consistent with the dating results of both overlying samples and with and age of 55 ± 6 ka obtained at 0.6m depth by Mokatse et al., 2022a. At the ACA site, the sample from 0.8 m depth yielded an age of 54 ± 5 ka, and the deepest carbonate bed at 4.6 m depth is dated to 163 ± 16 ka, which is synchronous (within uncertainty) with the deposition of the sand at 5.8 m depth at 137 ± 11.

Table 1. Dose rate assessment and age calculation. A value of 10 ± 3 wt% water was assigned to all samples expect from waterlogged samples where 21 ± 3 wt% values were assigned. The cosmic dose rate of the sand samples (below the carbonate layers) was modelled according to the thickness of sand and carbonate units and the time of emplacement of overlying layers. See Supporting Information for further details.

Sample	Depth [m]	Generalized content	U [ppm]	Th [ppm]	K [%]	Cosmic $\dot{D}$ [Gy ka^{-1}]	Total $\dot{D}$ [Gy ka^{-1}]	Overdispersion [%]	CAM De [Gy]	Age [ka]
ACA 0.8	0.8	Carbonate + sand	0.35 ± 0.09	0.29 ± 0.18	0.045 ± 0.005	0.219 ± 0.020	0.348 ± 0.027	22 ± 2	18.71 ± 0.82	54 ± 5
ACA 4.6	4.6	Carbonate + sand	0.83 ± 0.22	1.08 ± 0.33	0.100 ± 0.014	0.159 ± 0.016	0.482 ± 0.040	30 ± 4	78.51 ± 4.44	163 ± 16
ACA 5.8	5.8	Sand	0.85 ± 0.10	1.59 ± 0.09	0.158 ± 0.021	0.142 ± 0.014	0.551 ± 0.027	34 ± 4	75.27 ± 4.77	137 ± 11
ACA 6.3	6.3	Sand	0.80 ± 0.11	1.53 ± 0.28	0.088 ± 0.013	0.138 ± 0.014	0.472 ± 0.027	31 ± 3	71.92 ± 4.04	152 ± 12
ACA 7.0	7	Waterlogged sand	0.50 ± 0.10	0.93 ± 0.12	0.049 ± 0.009	0.133 ± 0.013	0.314 ± 0.020	32 ± 4	25.46 ± 1.46	81 ± 7
BP 5.5	5.5	Sand	0.44 ± 0.12	0.80 ± 0.12	0.116 ± 0.016	0.142 ± 0.014	0.383 ± 0.026	22 ± 2	57.21 ± 2.53	150 ± 12
BP 6.2	6.2	Sand	0.36 ± 0.13	0.47 ± 0.19	0.061 ± 0.009	0.136 ± 0.014	0.292 ± 0.026	31 ± 3	51.32 ± 3.58	150 ± 16
BP 6.8	6.8	Sand	0.34 ± 0.11	0.49 ± 0.15	0.053 ± 0.008	0.132 ± 0.013	0.278 ± 0.023	36 ± 4	43.86 ± 2.40	201 ± 20
BP 7.6	7.6	Sand	0.60 ± 0.12	0.81 ± 0.07	0.033 ± 0.006	0.127 ± 0.013	0.328 ± 0.023	35 ± 4	55.99 ± 3.39	116 ± 11

BP 8.3	8.3	Sand	0.16 ± 0.08	0.31 ± 0.12	0.019 ± 0.004	0.122 ± 0.012	0.190 ± 0.018	27 ± 3	55.99 ± 3.39	252 ± 27
BP 10	10	Waterlogged sand	0.71 ± 0.06	1.34 ± 0.18	0.094 ± 0.012	0.112 ± 0.011	0.389 ± 0.018	27 ± 3	47.87 ± 2.42	203 ± 14
NATA 0.8	0.8	Carbonate + sand	0.22 ± 0.10	0.16 ± 0.27	0.052 ± 0.006	0.212 ± 0.021	0.312 ± 0.029	15 ± 2	78.87 ± 3.99	74 ± 7
NATA 0.8 B	0.8	Carbonate + sand	0.36 ± 0.11	0.07 ± 0.26	0.055 ± 0.010	0.212 ± 0.021	0.338 ± 0.030	23 ± 2	23.14 ± 0.87	58 ± 6
NATA 2.0	2	Carbonate + sand	0.51 ± 0.12	0.34 ± 0.08	0.050 ± 0.008	0.191 ± 0.019	0.360 ± 0.027	21 ± 2	19.49 ± 0.87	64 ± 6
NATA 3.5	3.5	Sand	0.31 ± 0.07	0.95 ± 0.16	0.095 ± 0.015	0.171 ± 0.017	0.376 ± 0.024	23 ± 3	23.05 ± 0.99	143 ± 11
NATA 4.5	4.5	Waterlogged sand	0.31 ± 0.10	0.78 ± 0.02	0.048 ± 0.007	0.161 ± 0.016	0.298 ± 0.021	28 ± 3	53.74 ± 2.46	180 ± 16
NATA 5.0	5	Waterlogged sand	0.35 ± 0.10	0.48 ± 0.26	0.036 ± 0.006	0.157 ± 0.016	0.275 ± 0.023	31 ± 3	53.53 ± 2.77	94 ± 10
TSC 0.8	0.8	Carbonate + sand	0.52 ± 0.09	0.54 ± 0.26	0.099 ± 0.017	0.212 ± 0.021	0.438 ± 0.029	38 ± 4	25.81 ± 1.43	29 ± 3
TSC 2.0	2	Carbonate + sand	0.58 ± 0.14	0.40 ± 0.27	0.062 ± 0.010	0.191 ± 0.019	0.388 ± 0.032	19 ± 2	12.55 ± 0.79	81 ± 7
TSC 3.1	3.1	Sand	0.69 ± 0.11	1.44 ± 0.10	0.136 ± 0.021	0.176 ± 0.018	0.524 ± 0.029	29 ± 3	31.49 ± 1.31	116 ± 9
TSC 4.0	4	Sand	0.23 ± 0.09	0.56 ± 0.17	0.036 ± 0.006	0.166 ± 0.017	0.279 ± 0.023	35 ± 4	60.89 ± 3.19	139 ± 14
TSC 6.0	6	Sand	0.27 ± 0.11	0.58 ± 0.12	0.029 ± 0.005	0.149 ± 0.015	0.265 ± 0.023	20 ± 2	38.76 ± 2.30	199 ± 19

The ages of sand that underlie the carbonate layers were calculated assuming cosmic dose rate production during constant sedimentation rate and range between 252 ± 27 and 116 ± 9 ka (Table 1). Ages generally follow a stratigraphic order, apart from samples ACA 7.0, BP 10, and NATA 5.0. These outliers were saturated in water when sampled (discussed in Supporting Information).

5.2 Cosmogenic nuclides

Blank corrected concentrations of ^{26}Al and ^{10}Be of sand samples range from 1.18×10^6 to 14.03×10^6, and from 0.33×10^6 to 3.67×10^6 atoms g^{-1}, respectively (Table 2). Although distributed over a noticeable concentration range, $^{26}Al/^{10}Be$ ratios are clustered in a narrow spectrum between 3.5 and 4.7, not correlated with nuclides' concentrations, which are not correlated in turn with distance from the CE.

Kernel density estimates resulting from the Cosmolian model produce overall log-normal distributions and their weighted average value reflects the most probable surface residence time of each sand sample (Figure 4). While the different combinations of scenarios generally converge into a distinct peak, several samples present a bi-modal distribution with a relatively narrow combined range or positive skewness. These are probably the outcome of grains within the same sample with different sources and transportation histories (Vainer and Ben Dor, 2021), and this variance is reflected in the uncertainty estimation.

Residence time estimates for all analyzed samples span the time range between $0.91^{+0.24}/_{-0.22}$ and $2.22^{+0.96}/_{-0.69}$ Myr (Table 2). Their ages display a correlation (with r = 0.57) with distance from the CE, with ages being overall younger with proximity to the depocenter on the western margins

of the CE (Figure 4a). Simulations that were carried out with an overburden of 1 m (density of 1.7 g cm^{-3}) did not reach convergence with the measured values. This result agrees with the evoked mean value of the overburden required for simulations to converge with measured concentrations. This value is 4.7 ± 3.9 m if all samples are considered, or 5.0 ± 3.3 m if the two thinnest and two thickest simulated values of overburden are excluded (Table 2). Furthermore, the least likely assigned erosion rate during production in source areas is 3 m Ma^{-1}, in accordance with major sources in northern provinces where erosion rates are higher (Regard et al., 2016; Garzanti et al.,

2022).

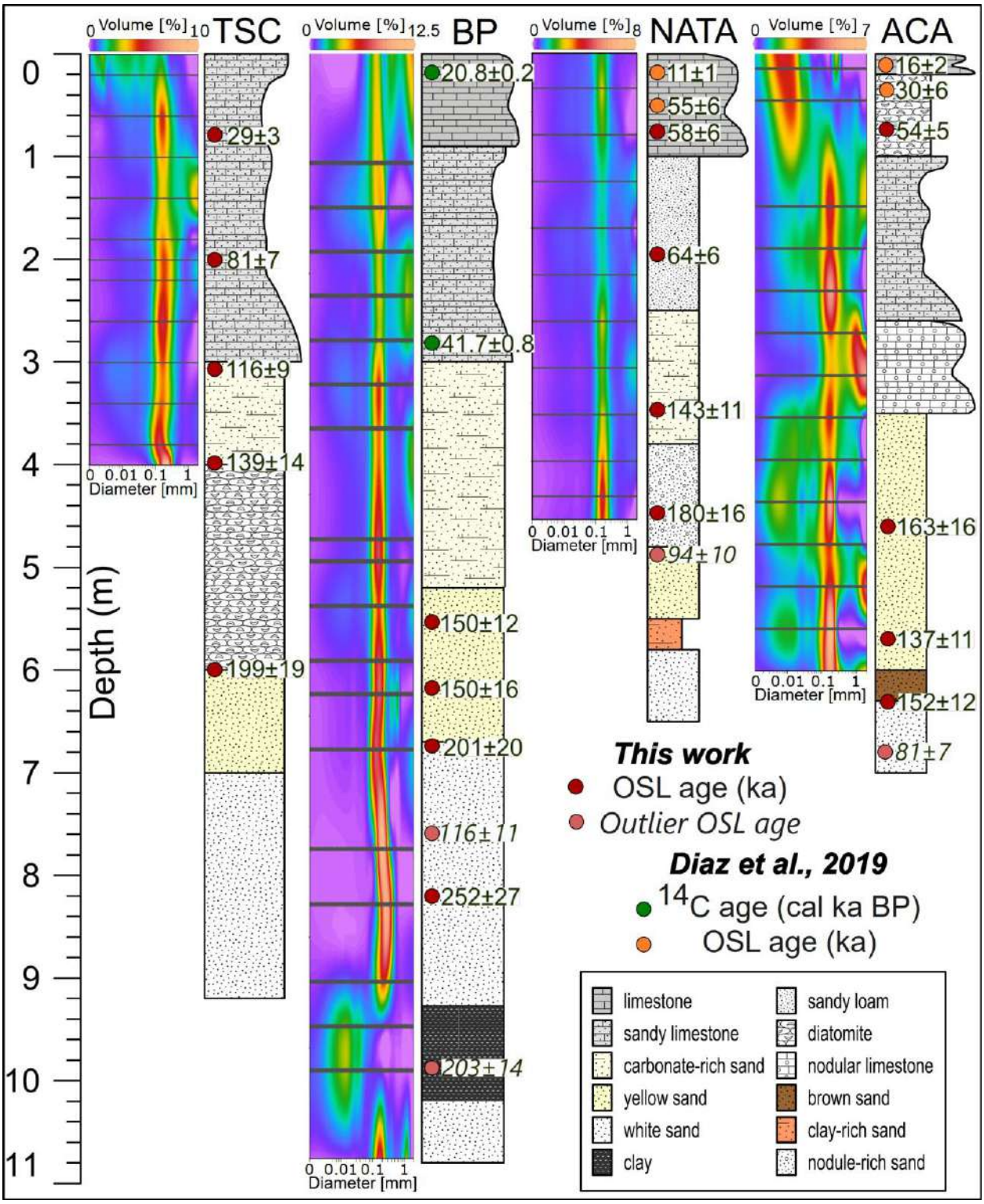

Figure 3 Lithology, grain size distribution, and chronology of deposits recovered from sampling pits dug in the Chobe Enclave.Grain size data points are represented by horizontal gray lines and were interpolated and plotted using ODV (Schlitzer, 2024) w. The locations of pits are shown in Figure 2.

5.3 Mineralogy

All analyzed sands are pure quartzose, with quartz representing 98-100% of the grain framework, with a few feldspars (almost exclusively K-feldspar) and rare mica. The very poor to extremely poor tHM suite consists mainly of tourmaline, associated with kyanite, zircon, and staurolite (Table 3). Rutile, epidote, titanite, hornblende, anatase, and brookite, are minor, sillimanite sporadic, and garnet and apatite are rare.

The mineralogical suite significantly differs (e.g., have much less zircon and epidote and much more staurolite and kyanite) from the assemblage that characterizes the regional Kalahari sand dunes (Table 3).. The ZTR index is 58±10, and the staurolite/kyanite ratio ranges between 0.4 and 1.2. Simple forward mixing calculations (Garzanti et al., 2012) and similarity analysis (Vezzoli and Garzanti, 2009) suggest subequal contributions from the Cuando and Uppermost Zambezi.

Table 2. Cosmogenic nuclides concentrations of sand samples from the Okavango Rift Zone (ORZ) and its vicinity and their simulated results given by the Cosmolian Model. The results shown include (1) the most probable average overburden (2) the ratio of successful simulations of vertical quartz grain displacement rates evoked from using fluvial, lacustrine, and palustrine (FLP) datasets for simulating vertical displacement rates vs. those from eolian datasets, and (3) the surficial residence time that represents the most probable time since the sediment was introduced into the landscape. Parameters used as input are detailed in Table S4, Supporting Information.

Sample	Current landform	Elevation [m]	$^{26}Al \times 10^{6}$ [at g^{-1}]	$^{10}Be \times 10^{6}$ [at g^{-1}]	$^{26}Al/^{10}Be$	Simulated overburden height [m]	Residence time [Myr]
PF	River	1016	1.44±0.18	0.34±0.01	4.2	7.4	$1.27\ ^{+0.43}/_{-0.32}$
A2	Dunefield	1127	3.93±0.18	1.03±0.04	3.8	4.5	$1.43\ ^{+0.34}/_{-0.25}$
KN	Dunefield	1064	2.63±0.14	0.70±0.02	3.7	5.2	$1.53\ ^{+0.32}/_{-0.27}$
MB	Dunefield	1072	1.18±0.15	0.33±0.02	3.5	7.1	$2.22\ ^{+0.96}/_{-0.69}$
KZ	River	977	3.14±0.19	0.68±0.02	4.6	4.8	$0.98\ ^{+0.25}/_{-0.26}$
KS20	Dunefield	1250	12.9±0.58	3.67±0.11	3.5	2.4	$2.17\ ^{+1.02}/_{-0.42}$
KS21	Dunefield	1217	3.0±0.15	0.77±0.03	3.9	5.6	$1.39\ ^{+1.48}/_{-0.24}$
KS23	Dune/river bank	1027	5.48±0.25	1.31±0.05	4.2	4.1	$1.14\ ^{+0.39}/_{-0.25}$
KS25	River	941	2.75±0.14	0.62±0.02	4.5	5.4	$1.04\ ^{+0.24}/_{-0.22}$
KS26	River	931	4.23±0.20	0.90±0.03	4.7	4.2	$0.91\ ^{+0.24}/_{-0.22}$
KS27	Sandsheet	962	14.03±0.61	3.28±0.10	4.3	2.0	$1.59\ ^{+0.8}/_{-0.37}$
KS28	Sandsheet	1249	4.38±0.20	1.18±0.05	3.7	4.3	$1.46\ ^{+0.35}/_{-0.26}$
KS29	Dunefield	1058	3.80±0.19	0.93±0.04	4.1	4.6	$1.27\ ^{+0.81}/_{-0.24}$

Table 3. Heavy mineral assemblages. Data of regional fluvial and eolian sand are after Garzanti et al. (2021) and (2022), respectively.

Sample	HMC w%	tHMC w%	zircon	tourmaline	rutile	Ti Oxides	titanite	apatite	epidote	garnet	staurolite	andalusite	kyanite	sillimanite	amphibole	clinopyroxene	others	ZTR	St/Ky
Chobe Enclave																			
TSC6.0	0.08	0.05	8	43	7	0	0	0	5	0	20	0	17	0	0	0	0	58	1.2
TSC6.8	0.10	0.06	17	35	4	0	0	0	2	0	19	0	21	1	0	0	0	56	0.9
BP5.5	0.83	0.47	17	32	7	0	0	0	6	0	13	0	24	0	0	0	0	57	0.5
BP10.0	0.22	0.13	12	33	3	2	5	0	4	0	10	0	29	0	0	0	0	48	0.4
ACA6.3	0.13	0.08	14	38	4	0	1	0	4	0	11	0	25	0	2	0	0	55	0.5
ACA7.0	0.19	0.09	17	37	7	0	2	0	5	0	13	0	22	0	1	0	0	60	0.6
NATA3.5	0.19	0.11	17	40	6	0	3	0	2	0	13	0	16	0	0	0	2	63	0.8
NATA5.0	0.21	0.11	18	41	10	0	0	1	6	1	9	0	16	0	1	0	0	68	0.6
Average																			
zircon 15±3 epidote 4 ± 1 staurolite 13 ± 4 kyanite 21 ± 5																			
Fluvial sand																			
I *Cuando*	0.07	0.03	24	27	6	0	1	0	4	0	19	1	11	0	5	0	0	57	1.8
II *Linyanti*	0.10	0.06	9	51	6	0	0	0	0	0	20	1	13	0	0	0	0	66	1.5
III *Chobe*	0.27	0.14	29	24	6	0	0	0	5	0	10	0	23	0	2	0	0	69	0.4
IV *Zambezi (Kazungula)*	0.39	0.25	22	15	6	0	0	0	8	1	7	0	36	1	3	0	0	43	0.2
V *Zambezi (Livingstone)*	0.52	0.23	18	16	5	2	0	1	12	0	4	1	27	0	4	14	0	39	0.1
VI *Zambazi (Sheshka)*	0.2	0.1	12	18	14	0	1	0.5	9	0	8	1	21	0.5	2	12	0	44	0.4
KZ	0.2	0.1	24	25	8	0.5	0	0	3	0.5	7	0	30	0.5	1	0	0	57	0.2
Average																			
zircon 20±7 epidote 6 ± 4 staurolite 11 ± 6 kyanite 23 ± 8																			
Kalahari Sand Dunes																			
KS27	0.3	0.3	33	18	7	0	0.5	0.5	28	5	2	0	1	0	1	6	0	58	1.5
KS28	0.5	0.1	47	34	5.5	0	0.5	0.5	0.5	0	10	0	1	0	0	1	0	87	10.5
KS29	0.3	0.1	40	43	5.0	0	0	0	1	0.5	8	0	2	0	0	1	0	88	4.5
KS30	0.6	0.3	36	15	6	0	0.5	0	40	1	0.5	0	1	0	0	0	0	57	0.3
Average																			
zircon 39±6 epidote 17 ± 20 staurolite 5 ± 5 kyanite 1 ± 0																			

6. Discussion

6.1 Deposits of the Cuando-Zambezi alluvial fans

The studied pits that are spread over a ~5 km^2 area (Figure 2e) reveal sedimentary sequences of spatio-temporal variations described below and illustrated in Figure 3, reflecting the diversity of depositional environments within a dynamic geomorphological system

(1) The basal sediments from all four pits comprise regionally continuous white sand, intercalated by muds with a phyllosilicate content ranging between 13-35% (Mokatse et al., 2023). The occurrence of > 70% clay sub-unit (most of which is a mixture of kaolinite and sepiolite) within the white sand at BP (Figure S8, Supporting Information) confirms deposition in a composite environment with markedly changing fluvial energy through time, as typical of alluvial fans (Stock, 2013). The ages of the strata above the white sand constrain the oldest deposits as not later than ~200-150 Ka, as also indicated by two OSL ages of the lower sand unit at BP that were buried at 252 ± 27 and 201 ± 20 Ka.

The deepest samples from BP, NATA, and ACA pits were taken from water-logged units using an auger drill and yielded ages out of stratigraphic order. Possible reasons for this age underestimation are discussed in the Supporting Information. Therefore, the earliest deposition at the studied sites is constrained to have occurred before 250 Ka.

(2) Yellow/brown sand overlying the white sand is observed at all sites, displaying some lateral variations and variations in carbonate content. Overall, the clay content in this unit ranges between 19 and 40 %; higher sepiolite abundance at the expense of kaolinite in comparison with the white sand below may imply some evaporitic conditions (Mokatse et al., 2023). The yellow sand facies was deposited between ~200 and 140 ka (199 ± 19 and 137 ± 11 ka; n = 5). At the ACA site, the yellow sand is different in nature than in the other sites as it is noticeably rich in carbonate and iron. This could indicate a reworked paleosol that may explain the age inversion observed at ACA (even though ages overlap within their analytical uncertainty), which could be also explained by bioturbation. At the NATA site, highly siliceous, bioturbated deposits accumulated at 180 ± 16 Ka. Between ~200 and 139 ± 14 Ka, a diatomite unit accumulated at TSC. These observations point to multiple depositional environments with a relatively large range of water depths and depositional energies, composition of solutes, and precipitation-to-evaporation ratios. These sub-environments were found in close proximity inside a dynamic alluvial fan setting.

(3) The diatomite and carbonate deposits that lie in unconformity above the sand below (Figure S8, Supporting Information) mark the initial deposition in a lacustrine environment that took place during the regionally wet MIS 5 (Burrough et al., 2009). Their deposition is constrained by three samples from two sites to have occurred after ~200 ka, with depositional ages of 143 ± 11 and 116 ± 9 Ka. Lateral and vertical calcite content changes (Mokatse et al., 2023), ranging from 0 to 4% at the NATA and TSC sites (where ages were determined), to ~50% at BP and ACA where age is defined only by correlation. The change from primary siliceous deposits that contain no carbonate to the deposition of carbonate implies a noticeable change in the chemistry

of the precipitating solution that could have resulted from an adjustment to morphotectonic or climatic shifts, as discussed below.

(4) A change in the environment occurred at 81 ± 7 ka and is synchronous with the global climatic perturbations and regional environmental changes of MIS 3 (e.g. Agostaand and Compagnucci, 2016; Stewart and Jones, 2016). A carbonate-rich palustrine/lacustrine environment is inferred from sediment micromorphology and due to the abundance of calcite at all sites, commonly representing the most abundant mineral (Diaz et al., 2019; Mokatse et al., 2023). The upper units at the NATA and ACA sites, which lie ~0.5 km from each other, are constrained by six OSL ages ranging from 58 ± 6 and 11 ± 1 ka. While carbonate is the main precipitate at NATA around 50 ka, diatomites and clays (with high sepiolite content) were deposited at ACA, pointing to less alkaline conditions locally, possibly related to pluvial lake settings. These sediments resemble surficial deposits of the Okavango Delta that originate from semi-continuous flood events under semi-arid conditions and desiccation. In the Okavango Delta, silicious and carbonate-rich precipitates are discretely deposited, and while carbonate minerals are present, they are far less common in the Okavango Delta than in the CE (McCarthy and Ellery, 1995; Ringrose et al., 2008; Dauteuil et al., 2021). These differences raise the question of the composition and origin of the parent solutions of the water flows in the CE during the later Pleistocene.

6.2 Provenance

The mineralogical assemblages of all buried CE samples imply similar sources, represented by a mixture of sediments presently carried by the Zambezi and Cuando rivers that drain northern terrains (Garzanti et al., 2021). This could be the result of the inter-basin hydrological connectivity with the Zambezi River that changes naturally as drainages are separated or combined through avulsion and due to external forces, such as climate change and tectonic activity (Shaw and Thomas, 1992; Wilkinson et al., 2023). Furthermore, XRD patterns of the studied samples reveal that non-carbonate mud samples (Figure S8, Supporting Information) contain 14-46 % phyllosilicates (Mokatse et al., 2023), congruent with a primary fluvial/alluvial transporting agent. Moreover, kyanite enrichment in sediments carried by the Chobe River (the spill of the Cuando into the CE) across the CE, relative to the upper reaches of the Cuando, points to the incorporation of fluvial sediments from the Upper Zambezi by the Chobe, and their reworking from deposition in alluvial fan settings (Garzanti et al., 2022; Mokatse et al., 2022b). A northern source is also suggested for the surficial sand that is carried by rivers into the MOZB as it presents a significantly higher success rate of Cosmolian simulations by applying displacement rates constructed from the FLP rather than the eolian dataset rates (Table 2). This sand (samples KS25, KS26) has ≤ 2% success in Cosmolian convergence events for scenarios with an erosion rate of 3 m Ma^{-1} that characterizes southern source areas, while higher erosion rates that characterize northern areas yield higher successful scenarios. This pattern of simulations resembles the simulations of northern dune sand and river samples (MB, KZ, PF, KS21) that arrive from areas with higher erosion rates (Garzanti et al., 2022) and differ from the rest of the sand samples to the south that present noticeable convergence also for scenarios with slower eroding source areas (Figure 4b). Furthermore, a coupled fluvial-eolian transport agent is

554 deduced also for currently eolian dune samples (Garzanti et al., 2022), as all modelled samples
555 experienced successful simulations by applying rates from both FLP and eolian datasets.

556 Although some mineralogical similarity exists with sand dunes located on the upper reaches of
557 the Zambezi, the mixed source for the buried CE sediments differs from sources that
558 predominate the Kalahari sand dunes as well as from their diagenetic history (Table 3). Their
559 differences in nature and age are reflected in their colors. The sand in the CE is mostly white and
560 yellow (Figure 3; Supporting Information S8) resulting from secondary iron oxyhydroxides
561 coating, likely due to hydration under alkaline conditions during fluvial transportation.
562 Conversely, the eolian Kalahari Sand is red (Wang et al., 2007) due to longer pedogenesis with
563 rubificataing edaphic conditions (Walker and McKee, 1979). Hence, whereas the modes of the
564 grain size distribution of CE sands and Kalahari sand lie within the same range (Mokatse et al.,
565 2022a), they do not share a genetic link and do not represent re-deposition of Kalahari dunes.
566 Additional observations point to fluvial incision and transport of material from elsewhere that
567 postdates the establishment of the dunes. These observations include (1) the offset and truncation
568 of dunes west of the Okavango Delta by faults and the lowering of base level associated with the
569 subsidence of the MOZB (McFarlane and Eckardt, 2007); and (2) the flow of the Gwayi River
570 parallel to the crests of linear dunes in the eastern MOZB (Figure 2a) (Thomas and Shaw, 1991;
571 Moore et al., 2012). Thus, the reason for the different mineralogical and textural signatures
572 between the Kalahari Sand and the CE buried sediments is probably the subsidence of the CE
573 and the incision of rivers into it (after the fixation of the eolian sand) (Figure 2d), carrying
574 sediment from their headwaters in a significantly greater proportion than recycled eolian sand
575 from their riverbanks.

576 6.3 Sand chronology

577 Eolian sand within the MOZB was exhumed between 2.22 $^{+0.96}/_{-0.69}$ and 1.14 $^{+0.39}/_{-0.25}$ Ma,
578 marking the upper age limit for the last significant geomorphologically evident subsidence event
579 in the CE, as no sand with similar sources and diagenetic history is found in the CE. The
580 distribution of the mean residence times of all sand samples correlates moderately ($r = 0.6$) with
581 elevation and increases with distance from the Linyanti-Chobe Basin ($r = 0.57$) (Figure 4a,c).
582 Collectively, this points to the preservation of the older sediments on the higher margins of the
583 tectonic trough of the CE and the incorporation of more recently eroded material downwards into
584 the evolving basin.

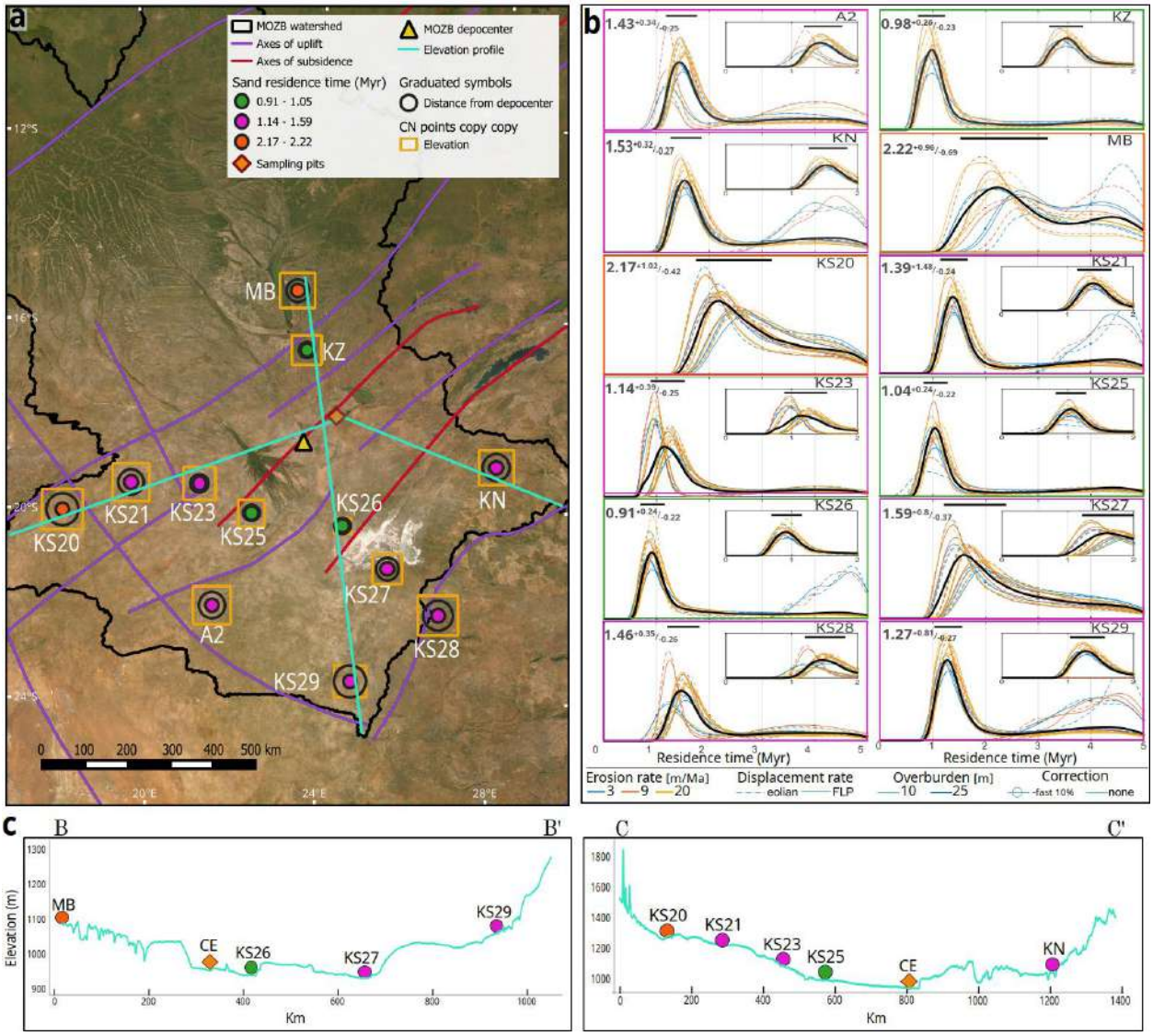

Figure 4. (a) Sands of the Makgadikgadi–Okavango–Zambezi Basin are categorized into three groups based on their sedimentary residence time. Simplified structural axes highlight the multi-block configuration (Haddon and McCarthy, 2005) overlying a satellite image of central southern Africa (ESRI, 2023). The size of the graduated symbols increases with larger values. (b) Kernel density estimates of the sedimentary residence time of sands, simulated with the Cosmolian Model (Vainer et al., 2018a; Vainer and Ben Dor, 2021). The probability plots show successful runs in which simulated concentrations of ^{26}Al and ^{10}Be simultaneously matched with their analytical values. 10,000 iterations were applied for each combination of the boundary conditions. The various scenarios include three values of erosion rate at the source areas, vertical displacement rates constructed from accumulation ages of either eolian or Fluvial-Lacustrine-Pluvial (FLP) datasets, and three values representing different transportation agents that resolve in changeable overburden thickness. The weighted average of the matching simulations is shown with a black solid line with uncertainty marked by the horizontal line on top, calculated with full-width at the half-maximum approach. The simulations performed for the PF sample are not shown due to a <1% success rate. (c) Elevation profiles of two nearly perpendicular cross sections across the basin, passing through the Chobe Enclave, constructed from 30 m DEM (Farr et al., 2007).

The Jenks natural breaks optimization highlights three periods of sand introduction that also roughly correspond to their structural position with respect to the CE and their geomorphological

context (fluvial/eolian) at present (Figure 4). (1) Sand collected in fluvial settings near the CE depocenter belongs to the youngest age group with mean ages in the range of 1.05-0.91 Ma (n = 3). This excludes additional input from the Okavango River (PF) that yielded less than 1% of successful simulations with a mean age of $1.27^{+0.43}_{-0.32}$ Ma. In the subsurface of the western MOZB, sediments younger than ~1.1 and 1.4 Ma are not preserved in the downthrown and upthrown blocks, respectively (Vainer et al., 2021). The absence of buried deposits younger than ~1 Ma and the lack of sand production since that time suggest a re-organization affecting the interconnection between the fluvial and eolian systems around 1 Ma. The paucity in sediment burial after ~1 Ma is observed throughout the southern Kalahari, suggesting the beginning of a primary regional eolian phase (excluding the ORZ), following tectonic uplift of the Kalahari margins (Matmon et al., 2015; Vainer et al., 2018b). (2) Eolian sand located on the surface that is just above the CE yielded mean residence time ages of 1.59-1.14 Ma (n = 7). During this period, sand from eolian landforms located ~50-300 km to the south and southwest of the MOZB water divide was extensively formed (Vainer et al., 2022), pointing to a regional (over the MOZB limits) phase of sand production. (3) The most distal to the CE eolian sand was exhumed around 2.2 Ma (n=2; Figure 4). The initial sand supply into the MOZB coincides with the deposition of basal eolian sand characterized by eolian grain size distribution in the southwestern Kalahari between $2.2^{+0.18}/_{-0.17}$ and $1.74^{+0.15}/_{-0.15}$ Ma (Vainer et al., 2022) and with distinct hydrological changes in the western Kalahari at ~2 Ma (Miller et al., 2010). Together, this chronology points to Kalahari Basin-scale changes that resulted in the initiation of sand cover and its eolian distribution around 2.2 Ma.

6.4 Landscape evolution of the Okavango Rift Zone since the Pleistocene

The chronology of landscape evolution in the ORZ is addressed via two dating methods that differ by an order of magnitude in their dating capabilities, allowing temporally constraining the rifting before and after the last significant phase of subsidence in the CE. The chrono-structural development of the ORZ can be tracked through the relationships between sedimentation and geomorphology, hinting at the stages of morphodynamical evolution of the nascent rifting zone (Figures 4, 5). Two elevation profiles that pass through the CE illustrate a symmetric (N-S, E-W) structural-block development during continental rifting (Holz et al., 2017), with the oldest sediments deposited at ~2.2 Ma. The two sites, where sand of this age is present, are located on elevated landforms on the outer-most structural blocks with respect to the CE. These sands could have been generated due to erosion following relief forming in the MOZB by virtue of tectonics at ~2.5 Ma (Thomas and Shaw, 1990; McCarthy et al., 2002; Moore et al., 2012; Vainer et al., 2021). A more recent tectonic activity resulted in the formation of a lower base level, enabling the preservation of older sand on the surface of the elevated landforms (Figures 2c, 5).

The inner lower blocks that lie above the CE accommodate sand that was formed at ~1.6-1.1 Ma, representing a second phase in landscape lowering and deformation. Tectonism at ~1.4 Ma was biochronologicaly inferred from the lacustrine radiation of tigerfish in the MOZB (Goodier et al., 2011) and was claimed by Moore et al. (2012) to cause changes in the configuration of the MOZB hydrological system. Such a change is also observed in the chrono-stratigraphy of the sand, as no sand that is found today in eolian settings has been produced since. Therefore, this timing signifies the earliest date for subsidence and formation of accommodation space in the CE. Finally, the successful modelling efforts of the fluvial sand indicate that it was exhumed around ~1 Ma, pointing to a change in the depositional environments that possibly resulted from

a new structural configuration occurring around the same time (Matmon et al., 2015; Vainer et al., 2018b), concurrent with the Middle Pleistocene Transition (MPT, 1.2-0.75 Ma; Herbert, 2023).

Burial ages of basal deposits in the CE could indicate the timing of the last significant rifting stage. However, such deposits were not reached in this work, and thus direct dating of the earliest sedimentation in the CE could not be achieved. We could only determine that accommodation space in the CE was available after 1.1 Ma and before 0.25 Ma. Sedimentary sequences deposited during continental rifting may overlie volcanic or basement rocks and typically consist of gravel, followed, or intercalated by fluvio-deltaic sands, overlain in turn by lacustrine and evaporitic deposits (Olsen et al., 1996; Young et al., 2000; Nielsen et al., 2007). The syn-rift sequence described in this study lacks basal conglomerate and begins with alluvial sand. In accordance with the isopach map of Haddon and McCarthy (2005), the unreached sedimentary suite below the studied pits in the CE is possibly 20-50 m thick. Assuming similar accumulation rates to those of the dated sediments, and accounting for the estimated missing thickness range, it is speculated that sedimentation in the CE may have started closer to 1 Ma than to 0.25 Ma.

Several observations point to the existence of a topographic depression since ~1 Ma in the MOZB, where waterbodies were sustained and linked to tectonic-induced landscape evolution (Grove, 1969; Moore et al., 2012) (Figure 5). (1) Phylogeographic records of catfishes point to their radiation in a lacustrine environment at 0.9 ± 0.5 Ma. (Day et al., 2009; Cotterill and De Wit, 2011) (2) Early Stone Age (ESA) artifacts with a minimum age of 0.5 Ma were found in paleo lacustrine settings (McFarlane and Segadika, 2001; McFarlane and Eckardt, 2006; Moore and Cotterill, 2007) (3) Gravels containing ESA artifacts were found <10 km downstream the Victoria Falls (Figure 2), indicating the initiation of gorge incision due to lacustrine overtop from the MOZB into the Zambezi River at 1.1-0.65 Ma (Clark, 1950; Moore and Cotterill, 2010). The existence of this waterbody (or waterbodies) in the CE cannot be determined with the findings of this study.

The earliest dated waterbody deposits in the CE are diatomite and carbonate which accumulated at ~140 ka (Figure 3). This waterbody could have extended some 300 km to the southwest to Paleolake Ngami, where partially cemented lakebed deposits and coarse sand interpreted to represent a beach ridge accumulated at 133 ± 12 and 140 ± 11 ka, respectively (Shaw et al., 2003; Burrough et al., 2007). This timing also correlates with the earliest constrained high lake level stand at Palaeolake Makgadikgadi (~300 km to the south) which took place at 131 ± 11 ka (Burrough et al., 2009). The Paleolake Ngami and Paleolake Makgadikgadi sediments that were deposited during MIS 5 were chronologically linked to humid environmental conditions. This was based on synchronous speleothem growth in Drotsky's Cave, located ~ 400 km to the west, on the western ORZ uplifted (Burrough et al., 2007) and with distant high lake level stands in northern Hemisphere EARS valleys (> 2000 km) and the Sahara (> 5000 km) (Burrough et al., 2009). This agrees with our observations of synchronous deposition of silica nodule-rich sands, diatomites, and carbonate-rich sands, reflecting stability in water flux and positive hydrological excursions. Furthermore, with the termination of high lake stands in Paleolake Ngami and Palaeolake Makgadikgadi, drying conditions that commenced at 110 ka following a wet period were inferred based on thermoluminescence dating and geochemical study of duricrusts in the Makgadikgadi Basin (Ringrose et al., 2005; Ringrose et al., 2009). Accordingly, a transition

from a clast-dominated to chemical-dominated accumulation took place in the CE between 116 ± 9 and 81 ± 7 ka. However, speleothem precipitation occurs in arid conditions such that its paleoclimatic interpretation is better constrained with additional proxies (Vaks et al., 2010). Furthermore, volcanism and magmatism of the mid-late Pleistocene took place in the western and eastern sectors of the EARS (Michon et al., 2022), possibly affecting the palaeohydrological interpretation of the EARS-referred lakes (in the Magadi-Natron and Turkana basins). Moreover, structural displacement along the northern MOZB flanks was also proposed to occur between 300 and 100 Ka, based on the preservation of archaeological artifacts of this age on paleo-Makgadikgadi lakebeds. This was interpreted to cause the deflection of the Cuando River from the Makgadikgadi Basin into the CE, forming a waterbody (Moore and Larkin, 2001; Moore et al., 2012). Hence, both tectonic and climatic forcings could have shaped the evolution of the hydrological system of the MOZB, and its chronology is currently not sufficient to determine the timing of rift formation.

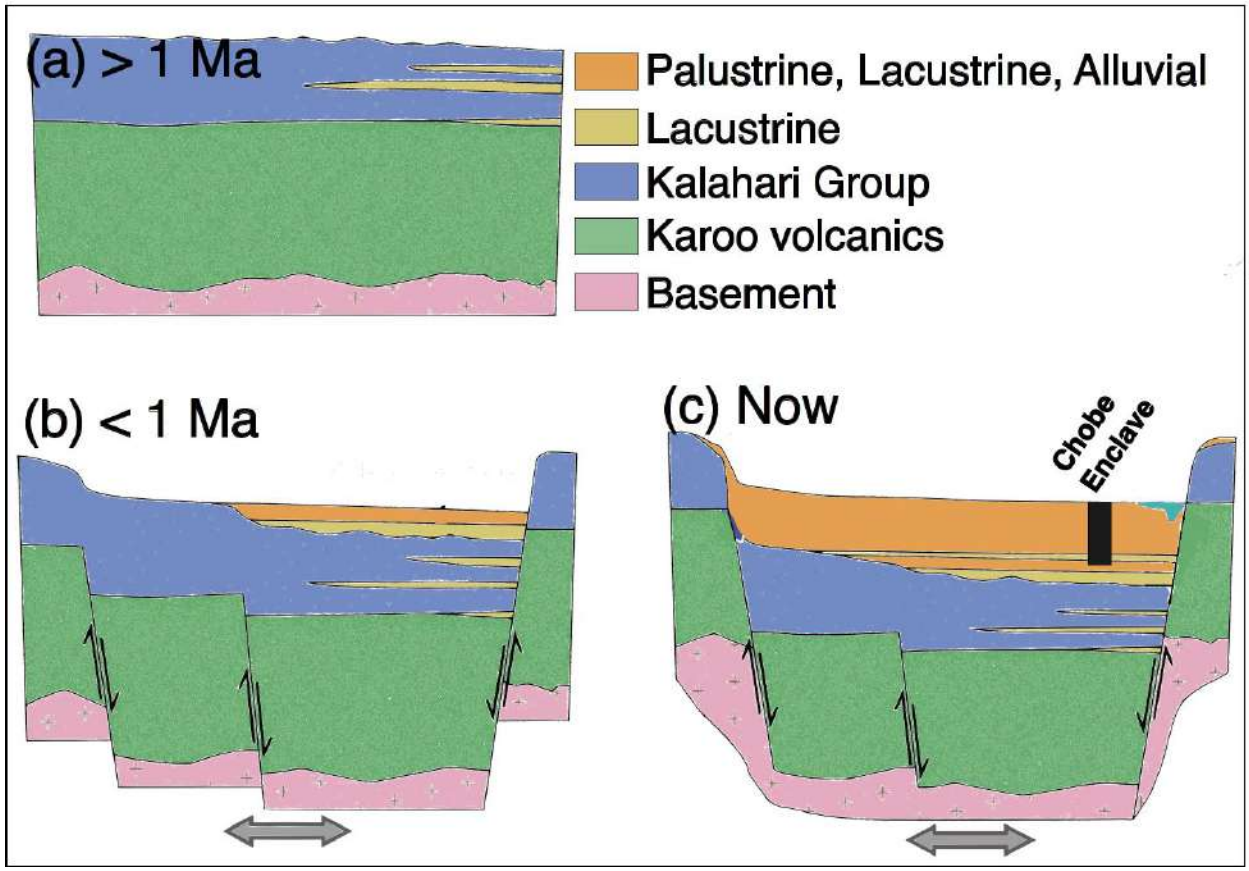

Figure 5. Conceptual model of the temporal coupling between the structural evolution and sedimentation in the ORZ (after Bäumle et al., 2019). The black bar represents borehole locations.

The last phase of carbonate precipitation and diatomite deposition in the CE documents an enduring waterbody that existed between 54 ± 5 and 11 ± 1 ka (Table 1, Figure 3). Lacustrine deposits from this period, centered at ~40 ka, were reported from all MOZ basins (summarized

in Burrough et al., 2009), hinting at a vast expansion of the lacustrine/palustrine system. Holocene sediments have not been observed in the studied sections, and their absence is consistent with the climatically driven desiccation of a waterbody in the Makgadikgadi Basin in the early Holocene (Partridge et al., 1997; Burrough et al.,2009), possibly resulting in their erosion. Alternatively, such deposits could have also been removed due to the activation of faults that occurred at ~6 ka in the CE, causing the diversion of drainage networks and inverted relief (Mokatse et al., 2022).

7. Conclusions

A combination of a mineralogical provenance study, optically stimulated luminescence (OSL) dating of alluvial and lacustrine deposits, and cosmogenic nuclide-based estimation of sand residence time was applied to chronologically constrain the landscape evolution in the Chobe Enclave, a tectonically active sector of the Okavango Rift Zone. The Chobe Enclave adjoins the thickest depocenter in the Makgadikgadi–Okavango–Zambezi Basin, which experienced significant down-warping at ~2.5 Ma. Cosmogenic nuclide-based modelling indicates that sand that was formed following this event is preserved on the elevated margins of the Makgadikgadi–Okavango–Zambezi Basin. Model results further suggest an additional event of landscape lowering occurring around 1.5 Ma, which probably corresponds to regional tectonism as most of the eolian Kalahari Sand was formed around this time and has been recycled since then in the semi-endorheic Kalahari Basin. This stage was followed by the accommodation of waterbodies within the Makgadikgadi–Okavango–Zambezi Basin, where their deposits of upper Pleistocene age are preserved. The last estimated episode of sand formation at 1.1 Ma marks the older limit for localized rifting in the Chobe Enclave, which probably occurred during the Middle Pleistocene Transition that took place between 1.2 and 0.75 Ma (Herbert, 2023).

Alluvial fans and waterbodies evolved within the depressed landscape of the Chobe Enclave, and their mineralogical signature suggests supply from both Zambezi and Cuando rivers, influenced by hydrological connectivity, climate, and tectonic activity. This alluvial system carried sand of different origin and diagenetic history than the older eolian sand that is structurally placed above the Chobe Enclave. Dating the alluvial sediments that were deposited in the evolved rift via OSL provided a younger time constraint for the incision. The earliest documented sedimentation in alluvial fan settings is dated as 252 ± 27 ka, representing the youngest age limit for a rifting episode in the Chobe Enclave. Finally, the subsidizing trough of the Chobe Enclave hosted waterbodies for at least ~140 ka, which were possibly connected with other waterbodies within the Makgadikgadi–Okavango–Zambezi Basin.

8. Acknowledgments

We are grateful for the preparation of cosmogenic nuclides, the practical comments, and the field missions conducted by Ari Matmon. We share our gratitude to Guy Lang, Vincent Regard, and Sebastien Carretier for fruitful discussions and comments, Yigal Erel, Talila Kosh, Ehud Rudis, and Izhak Temkin for their company, guidance, and cooperation in the field, the Van Thuyne Ridge research center for their hospitality and logistic support, and the Botswana International

University of Science and Technology for their fieldwork assistance. This work has been supported by a Swiss National Science Foundation grant no. 200021_172944 to E.P.V.

Open Research

Unless mentioned otherwise, the data presented in this paper is original. Mixing and similarity analyses based on mineralogical assemblages were performed after Garzanti et al. (2012) and Vezzoli and Garzanti (2009), respectively. OSL modelling for estimating dose rate and depositional age was performed via Mauz and Hoffmann (2014) Kreutzer et al. (2012, 2019, 2022), and Duller (2015). Cosmogenic nuclides modelling for residence time estimation was done using Cosmolian (Vainer and Ben Dor, 2021).

References

763 Agosta, E.A. and Compagnucci, R.H., 2016. Abrupt climate changes during the marine isotope
764 stage 3 (MIS 3). Marine Isotope Stage 3 in Southern South America, 60 KA BP-30 KA BP,
765 pp.81-106.

766 Andò, S., Garzanti, E., 2014. Raman spectroscopy in heavy-mineral studies. In: Scott, R.A.,
767 Smyth. H.R., Morton, A.C., Richardson, N. (Eds.), Sediment provenance studies in hydrocarbon
768 exploration and production. Geological Society London, Special Publication 386, 395-412.

769 Baillieul, T.A., 1975. A reconnaissance survey of the cover sands in the Republic of Botswana.
770 Journal of Sedimentary Research, 45(2), pp.494-503.

771 Bäumle, R., Himmelsbach, T. and Noell, U., 2019. Hydrogeology and geochemistry of a
772 tectonically controlled, deep-seated and semi-fossil aquifer in the Zambezi Region (Namibia).
773 Hydrogeology Journal, 27(3), pp.885-914.

774 Blair, T.C. and McPherson, J.G., 2009. Processes and forms of alluvial fans. In: Parsons, A.J.,
775 Abrahams, A.D. (eds) Geomorphology of Desert Environments. Springer, Dordrecht pp.413-467.

776 Bowman, D., 2019. Principles of alluvial fan morphology. Dordrecht: Springer, pp.151

777 Brook, G.A., Cowart, J.B., Brandt, S.A., 1998. Comparison of Quaternary environmental change
778 in eastern and southern Africa using cave speleothem, tufa and rock shelter sediment data.
779 Quaternary Deserts and Climate Change. G. Alsharhan, Whittle and Kendall. Rotterdam,
780 Balkema.

781 Brook, G.A., Srivastava, P., Brook, F.Z., Robbins, L.H., Campbell, A.C. and Murphy, M.L.,
782 2008. OSL chronology for sediments and MSA artefacts at the Toteng quarry, Kalahari Desert,
783 Botswana. South African Archaeological Bulletin, 63(188), pp.151-158.

784 Brown, N.D., 2020. Which geomorphic processes can be informed by luminescence
785 measurements?. Geomorphology, 367, p.107296.

786 Bufford, K.M., Atekwana, E.A., Abdelsalam, M.G., Shemang, E., Atekwana, E.A., Mickus, K.,
787 Moidaki, M., Modisi, M.P. and Molwalefhe, L., 2012. Geometry and faults tectonic activity of
788 the Okavango Rift Zone, Botswana: Evidence from magnetotelluric and electrical resistivity
789 tomography imaging. Journal of African Earth Sciences, 65, pp.61-71.

790 Burrough, S.L. and Thomas, D.S., 2013. Central southern Africa at the time of the African
791 Humid Period: a new analysis of Holocene palaeoenvironmental and palaeoclimate data.
792 Quaternary Science Reviews, 80, pp.29-46.

793 Burrough, S.L. and Thomas, D.S.G., 2008. Late Quaternary lake-level fluctuations in the
794 Mababe Depression: Middle Kalahari palaeolakes and the role of Zambezi inflows. Quaternary
795 Research, 69(3), pp.388-403.

796 Burrough, S.L., Thomas, D.S., Shaw, P.A. and Bailey, R.M., 2007. Multiphase quaternary
797 highstands at lake Ngami, Kalahari, northern Botswana. Palaeogeography, Palaeoclimatology,
798 Palaeoecology, 253(3-4), pp.280-299.

Chorowicz, J., 2005. The east African rift system. Journal of African Earth Sciences, 43(1–3), 379–410.

Clark, J.D., 1950. Part II – Archaeology. In: J.D. Clark (Editor), The Stone Age cultures of Northern Rhodesia. Southern African Archaeological Society, Claremont, 30-131.

Cosgrove, G.I., Colombera, L. and Mountney, N.P., 2022. Quantitative analysis of aeolian stratigraphic architectures preserved in different tectonic settings. Earth-Science Reviews, p.104293.

Cotterill, F.P.D. and De Wit, M.J., 2011. Geoecodynamics and the Kalahari epeirogeny: linking its genomic record, tree of life and palimpsest into a unified narrative of landscape evolution. South African Journal of Geology, 114(3-4), pp.489-514.

Daly, M.C., Green, P., Watts, A.B., Davies, O., Chibesakunda, F. and Walker, R., 2020. Tectonics and landscape of the Central African Plateau and their implications for a propagating Southwestern Rift in Africa. Geochemistry, Geophysics, Geosystems, 21(6), p.e2019GC008746.

Dauteuil, O., Jolivet, M., Dia, A., Murray-Hudson, M., Makati, K., Barrier, L., Bouhnik Le Coz, M., Audran, A. and Radenac, A., 2021. Trace metal enrichments in water of the Okavango Delta (Botswana): hydrological consequences. Geochemistry, Geophysics, Geosystems, 22(5).

Day, J.J., Bills, R. and Friel, J.P., 2009. Lacustrine radiations in African Synodontis catfish. Journal of evolutionary biology, 22(4), pp.805-817.

DeCelles, P.G. and Cavazza, W., 1999. A comparison of fluvial megafans in the Cordilleran (Upper Cretaceous) and modern Himalayan foreland basin systems. Geological Society of America Bulletin, 111(9), pp.1315-1334.

Degering, D., Degering, A., 2020. Change is the only constant - time-dependent dose rates in luminescence dating. Quaternary Geochronology 58, 101074.

Diaz, N., Armitage, S.J., Verrecchia, E.P. and Herman, F., 2019. OSL dating of a carbonate island in the Chobe Enclave, NW Botswana. Quaternary Geochronology, 49, pp.172-176.

Dixey, F. H., 1956. The East African Rift System. Colonial Geol. Mineral Resources, 1, pp. 1–71.

Doucouré, C.M. and de Wit, M.J., 2003. Old inherited origin for the present near-bimodal topography of Africa. Journal of African Earth Sciences, 36(4), pp.371-388.

Dumisani, J.H., 2001. Seismotectonics of Zimbabwe. African Journal of Science and Technology, 1(4).

Du Toit, A.L., 1933. Crustal movements as a factor in the evolution of South Africa. S. Afr. J. Sci. pp. 24, 88 – 101.

Duller, G.A.T., 2015. The Analyst software package for luminescence data: overview and recent improvements. Ancient TL, 33(1), pp.35-42.

Durcan, J.A., King, G.E., Duller, G.A.T., 2015. DRAC: Dose Rate and Age Calculator for trapped charge dating. Quaternary Geochronology 28, 54-61.

Eckardt, F.D., Cotterill, F.P., Flügel, T.J., Kahle, B., McFarlane, M. and Rowe, C., 2016. Mapping the surface geomorphology of the Makgadikgadi Rift Zone (MRZ). Quaternary International, 404, pp.115-120.

Esri. World Imagery Map. June, 2023.

Fairhead, J.D. and Girdler, R.W., 1969. How far does the rift system extend through Africa?. Nature, 221(5185), pp.1018-1020.

Farr, T.G., Rosen, P.A., Caro, E., Crippen, R., Duren, R., Hensley, S., Kobrick, M., Paller, M., Rodriguez, E., Roth, L. and Seal, D., 2007. The shuttle radar topography mission. Reviews of geophysics, 45(2).

Galbraith, R.F., Roberts, R.G., Laslett, G.M., Yoshida, H. and Olley, J.M., 1999. Optical dating of single and multiple grains of quartz from Jinmium rock shelter, northern Australia: Part I, experimental design and statistical models. Archaeometry, 41(2), pp.339-364.Garzanti E., 2017. The maturity myth in sedimentology and provenance analysis. Journal of Sedimentary Research, 87, 353-365.

Garzanti, E., Andò, S., 2007. Heavy-mineral concentration in modern sands: implications for provenance interpretation. In: Mange, M.A., Wright, D.T. (Eds.), Heavy Minerals in Use. Elsevier, Amsterdam, Developments in Sedimentology Series 58, pp. 517-545.

Garzanti, E., Pastore, G., Resentini, A., Vezzoli, G., Vermeesch, P., Ncube, L., Niekerk, H.J.V., Jouet, G. and Dall'Asta, M., 2021. The segmented Zambezi sedimentary system from source to sink: 1. Sand petrology and heavy minerals. The Journal of Geology, 129(4), pp. 343-369.

Garzanti, E., Pastore, G., Stone, A., Vainer, S., Vermeesch, P. and Resentini, A., 2022. Provenance of Kalahari Sand: Paleoweathering and recycling in a linked fluvial-aeolian system. Earth-Science Reviews, 224, p.103867.

Garzanti, E., Resentini, A., Vezzoli, G., Andò, S., Malusà, M., Padoan, M., 2012. Forward compositional modelling of Alpine orogenic sediments. Sedimentary Geology, 280, 149-164.

Gaudaré, L., Dauteuil, O. and Jolivet, M., 2024. Geomorphology of the Makgadikgadi Basin (Botswana): Insight Into the Propagation of the East African Rift System. Tectonics, 43(2), p.e2023TC007988.

Gierlowski-Kordesch, E.H., 2010. Lacustrine carbonates. Developments in sedimentology, 61, pp.1-101.

Goodier, S.A., Cotterill, F.P., O'Ryan, C., Skelton, P.H. and de Wit, M.J., 2011. Cryptic diversity of African tigerfish (Genus Hydrocynus) reveals palaeogeographic signatures of linked Neogene geotectonic events. PloS one, 6(12), p.e28775.

Grove, A.T., 1969. Landforms and climatic change in the Kalahari and Ngamiland. The Geographical Journal, 135(2), pp.191-212.

Guérin, G., Mercier, N., Adamiec, G., 2011. Dose-rate conversion factors: update. Ancient TL 29, 5-8.

Guérin, G., Combès, B., Lahaye, C., Thomsen, K.J., Tribolo, C., Urbanova, P., Guibert, P., Mercier, N., Valladas, H., 2015. Testing the accuracy of a Bayesian central-dose model for single-grain OSL, using known-age samples. Radiation Measurements 81, 62-70.

Gumbricht, T., McCarthy, T.S. and Merry, C.L., 2001. The topography of the Okavango Delta, Botswana, and its tectonic and sedimentological implications. South African Journal of Geology, 104(3), pp.243-264.

Haddon, I.G. and McCarthy, T.S., 2005. The Mesozoic–Cenozoic interior sag basins of Central Africa: the late-cretaceous–Cenozoic Kalahari and Okavango basins. Journal of African Earth Sciences, 43(1-3), pp.316-333.

Harvey, A. M., Stokes, M., Mather, A. and Whitfield, E., 2018. Spatial characteristics of the Pliocene to modern alluvial fan successions in the uplifted sedimentary basins of Almería, SE Spain: review and regional synthesis. Geological Society, London, Special Publications, 440(1), pp.65-77.

Harvey, A.M., 2002. The role of base-level change in the dissection of alluvial fans: case studies from southeast Spain and Nevada. Geomorphology, 45(1-2), pp.67-87.

Harvey, A.M., Mather, A.E. and Stokes, M., 2005. Alluvial fans: geomorphology, sedimentology, dynamics—introduction. A review of alluvial-fan research. Geological Society, London, Special Publications, 251(1), pp.1-7.

Herbert, T.D., 2023. The Mid-Pleistocene Climate Transition. Annual Review of Earth and Planetary Sciences, 51, pp.389-418.

Holz, M., Vilas-Boas, D.B., Troccoli, E.B., Santana, V.C. and Vidigal-Souza, P.A., 2017. Conceptual models for sequence stratigraphy of continental rift successions. In Stratigraphy & Timescales (Vol. 2, pp. 119-186). Academic Press.

Hooke, R.L., 1967. Processes on arid-region alluvial fans. The Journal of Geology, 75(4), pp.438-460.

Hubert, J.F., 1962. A zircon–tourmaline–rutile maturity index and the interdependence of the composition of heavy minerals assemblages with the gross composition and texture of sandstones. Journal of Sedimentary Petrology 32, 440-450.

Huntsman-Mapila, P., Kampunzu, A.B., Vink, B. and Ringrose, S., 2005. Cryptic indicators of provenance from the geochemistry of the Okavango Delta sediments, Botswana. Sedimentary Geology, 174(1-2), pp.123-148.

Huntsman-Mapila, P., Ringrose, S., Mackay, A.W., Downey, W.S., Modisi, M., Coetzee, S.H., Tiercelin, J.J., Kampunzu, A.B. and Vanderpost, C., 2006. Use of the geochemical and biological sedimentary record in establishing palaeo-environments and climate change in the Lake Ngami basin, NW Botswana. Quaternary International, 148(1), pp.51-64.

Keller, E.A. and DeVecchio, D.E., 2013. Tectonic geomorphology of active folding and development of transverse drainages. In Tectonic Geomorphology (pp. 129-147). Elsevier Inc..

Kinabo, B.D., Atekwana, E.A., Hogan, J.P., Modisi, M.P., Wheaton, D.D. and Kampunzu, A.B., 2007. Early structural development of the Okavango rift zone, NW Botswana. Journal of African Earth Sciences, 48(2-3), pp.125-136.

Kinabo, B.D., Hogan, J.P., Atekwana, E.A., Abdelsalam, M.G. and Modisi, M.P., 2008. Fault growth and propagation during incipient continental rifting: Insights from a combined aeromagnetic and Shuttle Radar Topography Mission digital elevation model investigation of the Okavango Rift Zone, northwest Botswana. Tectonics, 27(3), TC3013.

Kohl, C.P. and Nishiizumi, K., 1992. Chemical isolation of quartz for measurement of in-situ-produced cosmogenic nuclides. Geochimica et cosmochimica acta, 56(9), pp.3583-3587.

Kreutzer, S., Burow, C., Dietze, M., Fuchs, M., Schmidt, C., Fischer, M., Friedrich, J., Mercier, N., Philippe, A., Riedesel, S., Autzen, M., Mittelstrass, D., Gray, H., Galharret, J., 2022. Luminescence: Comprehensive Luminescence Dating Data Analysis. R package version 0.9.20, https://CRAN.R-project.org/package=Luminescence.

Kreutzer, S., Mauz, B., Martin, L., Mercier, N., 2019. 'RCarb': Dose Rate Modelling of Carbonate-Rich Samples-an Implementation of Carb in R. Ancient TL 37.

Kreutzer, S., Schmidt, C., Fuchs, M.C., Dietze, M., Fischer, M., Fuchs, M., 2012. Introducing an R package for luminescence dating analysis. Ancient TL 30, 1-8.

Lancaster, N., 1981. Paleoenvironmental implications of fixed dune systems in Southern Africa. Palaeogeography, Palaeoclimatology, Palaeoecology, 33(4), pp.327-346.

Le Dortz, K., Meyer, B., Sébrier, M., Braucher, R., Bourlès, D., Benedetti, L., Nazari, H. and Foroutan, M., 2012. Interpreting scattered in-situ produced cosmogenic nuclide depth-profile data. Quaternary Geochronology, 11, pp.98-115.

Lecce, S.A., 1990. The alluvial fan problem. In: A.H. Rachocki, M. Church (Eds) Alluvial fans: A field approach, Wiley, pp. 3-24.

Lustig, L.K., 1965. Clastic sedimentation in deep springs valley, California (Vol. 352). US Government Printing Office.

936 Mallick, D.I.J., Habgood, F., Skinner, A.C., 1981. A geological interpretation of Landsat
937 imagery andair photography of Botswana. Overseas Geology and Mineral Resources, 56, pp. 35.

938 Matmon, A., Hidy, A.J., Vainer, S., Crouvi, O., Fink, D., Erel, Y., Arnold, M., Aumaître, G.,
939 Bourlès, D., Keddadouche, K. and Horwitz, L.K., 2015. New chronology for the southern
940 Kalahari Group sediments with implications for sediment-cycle dynamics and early hominin
941 occupation. Quaternary Research, 84(1), pp.118-132.

942 Matmon, A., Nichols, K. and Finkel, R., 2006. Isotopic insights into smoothening of abandoned
943 fan surfaces, southern California. Quaternary Research, 66(1), pp.109-118.

944 Matmon, A., Schwartz, D.P., Finkel, R., Clemmens, S. and Hanks, T., 2005. Dating offset fans
945 along the Mojave section of the San Andreas fault using cosmogenic 26Al and 10Be. Geological
946 Society of America Bulletin, 117(5-6), pp.795-807.

947 McCarthy, T.S. and Ellery, W.N., 1995. Sedimentation on the distal reaches of the Okavango
948 Fan, Botswana, and its bearing on calcrete and silcrete (ganister) formation. Journal of
949 Sedimentary Research, 65(1a), pp.77-90.

950 McCarthy, T.S., 1993. The great inland deltas of Africa. Journal of African Earth Sciences (and
951 the Middle East), 17(3), pp.275-291.

952 McCarthy, T.S., 2013. The Okavango Delta and its place in the geomorphological evolution of
953 southern Africa. South African Journal of Geology, 116(1), pp.1-54.

954 McCarthy, T.S., Smith, N.D., Ellery, W.N., Gumbricht, T. 2002. The Okavango Delta - Semi-
955 arid alluvial fan sedimentation related to incipient rifting. In: Renaut R.W. and Ashley G.M.
956 (Eds), Sedimentation in Continental rifts. Society for Sedimentary Geology (SEPM), Special
957 Publication, 73, 179-193.

958 McFarlane, M.J. and Eckardt, F.D., 2006. Lake Deception: a new Makgadikgadi palaeolake.
959 Botswana Notes and Records, 38, pp.195-201.

960 McFarlane, M.J. and Eckardt, F.D., 2007. Palaeodune morphology associated with the Gumare
961 fault of the Okavango graben in the Botswana/Namibia borderland: a new model of tectonic
962 influence. South African Journal of Geology, 110(4), pp.535-542.

963 McFarlane, M.J. and Segadika, P., 2001. Archaeological evidence for the reassessment of the
964 ages of the Makgadikgadi palaeolakes. Botswana Notes and Records, 33, 83-89.

965 Messager, M.L., Lehner, B., Grill, G., Nedeva, I. and Schmitt, O., 2016. Estimating the volume
966 and age of water stored in global lakes using a geo-statistical approach. Nature communications,
967 7(1), p.13603. Data is available at www.hydrosheds.org.

968 Michon, L., Famin, V. and Quidelleur, X., 2022. Evolution of the East African Rift System from
969 trap-scale to plate-scale rifting. Earth-Science Reviews, 231, p.104089.

970 Miller, R.M., Pickford, M. and Senut, B., 2010. The geology, palaeontology and evolution of the
971 Etosha Pan, Namibia: Implications for terminal Kalahari deposition. South African Journal of
972 Geology, 113(3), pp.307-334.

973 Modisi, M.P., Atekwana, E.A., Kampunzu, A.B. and Ngwisanyi, T.H., 2000. Rift kinematics
974 during the incipient stages of continental extension: Evidence from the nascent Okavango rift
975 basin, northwest Botswana. Geology, 28(10), pp.939-942.

976 Modisi, M.P., 2000. Fault system at the southeastern boundary of the Okavango Rift, Botswana.
977 Journal of African Earth Sciences, 30(3), pp.569-578.

978 Mokatse, T., Diaz, N., Shemang, E., Van Thuyne, J., Vittoz, P., Vennemann, T. and Verrecchia,
979 E.P., 2022a. Landscapes and Landforms of the Chobe Enclave, Northern Botswana. In
980 Landscapes and Landforms of Botswana (pp. 91-116). Cham: Springer International Publishing.

981 Mokatse, T., Vainer, S., Irving, J., Schmidt, C., Kgosidintsi, B., Shemang, E. and Verrecchia,
982 E.P., 2022b. Geometry of sedimentary deposits and evolution of the landforms in the Chobe
983 Enclave, Northern Botswana. Geomorphology, 415, p.108406.

984 Moore, A.E. and Cotterill, F.P.D., 2010. Victoria Falls: Mosi oa Tunya – the smoke that
985 thunders. In: P. Mignon (Editor), Geomorphological Landscapes. Springer, Berlin, 143-153.

986 Moore, A.E. and Larkin, P.A., 2001. Drainage evolution in south-central Africa since the
987 breakup of Gondwana. South African Journal of Geology, 104(1), pp.47-68.

988 Moore, A.E., 1999. A reappraisal of epeirogenic flexure axes in southern Africa. South African
989 Journal of Geology, 102(4), pp.363-376.

990 Moore, A.E., Cotterill, F.P., Main, M.P. and Williams, H.B., 2007. The zambezi river. Large
991 rivers: geomorphology and management, pp.311-332.

992 Moore, A.E., Cotterill, F.P.D. and Eckardt, F.D., 2012. The evolution and ages of Makgadikgadi
993 palaeo-lakes: consilient evidence from Kalahari drainage evolution south-central Africa. South
994 African Journal of Geology, 115(3), pp.385-413.

995 Murray, A., Arnold, L.J., Buylaert, J.-P., Guérin, G., Qin, J., Singhvi, A.K., Smedley, R.,
996 Thomsen, K.J., 2021. Optically stimulated luminescence dating using quartz. Nature Reviews
997 Methods Primers 1, 1-31.

998 Murray, A.S. and Wintle, A.G., 2000. Luminescence dating of quartz using an improved single-
999 aliquot regenerative-dose protocol. Radiation measurements, 32(1), pp.57-73.

1000 Nash, D.J., Meadows, M.E. and Gulliver, V.L., 2006. Holocene environmental change in the
1001 Okavango Panhandle, northwest Botswana. Quaternary Science Reviews, 25(11-12), pp.1302-
1002 1322.

1003 Nathan, R.P., Mauz, B., 2008. On the dose-rate estimate of carbonate-rich sediments for trapped
1004 charge dating. Radiation Measurements 43, 14-25.

1005 Nielsen, L.H., Petersen, H.I., Thai, N.D., Duc, N.A., Fyhn, M.B.W., Boldreel, L.O., Tuan, H.A.,
1006 Lindstrom, S. and Hien, L.V., 2007. A Middle–Upper Miocene fluvial–lacustrine rift sequence in
1007 the Song Ba Rift, Vietnam: an analogue to oil-prone, small-scale continental rift basins.
1008 Petroleum Geoscience, 13(2), pp.145-168.

1009 Olsen, P.E., Kent, D.V., Cornet, B., Witte, W.K. and Schlische, R.W., 1996. High-resolution
1010 stratigraphy of the Newark rift basin (early Mesozoic, eastern North America). Geological
1011 Society of America Bulletin, 108(1), pp.40-77.

1012 Oriolo, S. and Becker, T., 2018. The Kalahari craton, southern Africa: from Archean crustal
1013 evolution to Gondwana amalgamation. Geology of southwest Gondwana, pp.133-159.

1014 Owen, L. A., Tectonic Geomorphology: A Perspective. Treatise on Geomorphology (Second
1015 Edition), pp. 1-12. https://doi.org/10.1016/B978-0-12-818234-5.00155-3

1016 ALOS PALSAR L1.0 2010. Accessed through ASF DAAC 23 March 2023.

1017 Partridge, TC & Maud, R.R., 1987. Geomorphic evolution of southern Africa since the
1018 Mesozoic. South African Journal of Geology, 90(2), pp.179-208.

1019 Partridge, T.C., 1993. The evidence for Cainozoic aridification in southern Africa. Quaternary
1020 International, 17, pp.105-110.

1021 Partridge, T.C., Demenocal, P.B., Lorentz, S.A., Paiker, M.J. and Vogel, J.C., 1997. Orbital
1022 forcing of climate over South Africa: a 200,000-year rainfall record from the Pretoria Saltpan.
1023 Quaternary Science Reviews, 16(10), pp.1125-1133.

1024 Pastier, A.M., Dauteuil, O., Murray-Hudson, M., Moreau, F., Walpersdorf, A. and Makati, K.,
1025 2017. Is the Okavango Delta the terminus of the East African Rift System? Towards a new
1026 geodynamic model: Geodetic study and geophysical review. Tectonophysics, 712, pp.469-481.

1027 Paulssen, H., Micallef, T., Bouwman, D.R., Ruigrok, E., Herman, M.W., Fadel, I., van der
1028 Meijde, M., Kwadiba, M., Maritinkole, J. and Ntibinyane, O., 2022. Rifting of the Kalahari
1029 Craton through Botswana? New seismic evidence. Journal of Geophysical Research: Solid Earth,
1030 127(4), p.e2021JB023524.

1031 Placzek, C.J., Matmon, A., Granger, D.E., Quade, J. and Niedermann, S., 2010. Evidence for
1032 active landscape evolution in the hyperarid Atacama from multiple terrestrial cosmogenic
1033 nuclides. Earth and Planetary Science Letters, 295(1-2), pp.12-20.

1034 Podgorski, J.E., Green, A.G., Kgotlhang, L., Kinzelbach, W.K., Kalscheuer, T., Auken, E. and
1035 Ngwisanyi, T., 2013. Paleo-megalake and paleo-megafan in southern Africa. Geology, 41(11),
1036 pp.1155-1158.

1037 Porat, N., Amit, R., Enzel, Y., Zilberman, E., Avni, Y., Ginat, H. and Gluck, D., 2010.
1038 Abandonment ages of alluvial landforms in the hyperarid Negev determined by luminescence
1039 dating. Journal of Arid Environments, 74(7), pp.861-869.

Reeves, C.V., 1972. Rifting in the Kalahari?. Nature, 237(5350), pp.95-96.

Regard, V., Carretier, S., Boeglin, J.L., Ngoupayou, J.R., Dzana, J.G., Bedimo, J.P., Riotte, J. and Braun, J.J., 2016. Denudation rates on cratonic landscapes: Comparison between suspended and dissolved fluxes, and 10Be analysis in the Nyong and Sanaga River basins, South Cameroon. Earth Surface Processes and Landforms, 41(12), pp.1671-1683.

Ringrose, S., Harris, C., Huntsman-Mapila, P., Vink, B.W., Diskins, S., Vanderpost, C. and Matheson, W., 2009. Origins of strandline duricrusts around the Makgadikgadi Pans (Botswana Kalahari) as deduced from their chemical and isotope composition. Sedimentary Geology, 219(1-4), pp.262-279.

Ringrose, S., Huntsman-Mapila, P., Downey, W., Coetzee, S., Fey, M., Vanderpost, C., Vink, B., Kemosidile, T. and Kolokose, D., 2008. Diagenesis in Okavango fan and adjacent dune deposits with implications for the record of palaeo-environmental change in Makgadikgadi–Okavango–Zambezi basin, northern Botswana. Geomorphology, 101(4), pp.544-557.

Ringrose, S., Huntsman-Mapila, P., Kampunzu, H., Downey, W.D., Coetzee, S., Vink, B., Matheson, W., Vanderpost, C., 2005. Geomorphological and geochemical evidence for palaeo feature formation in the northern Makgadikgadi sub-basin, Botswana. Palaeogeog. Palaeoclim. Palaeoecol. 217, 265–287.

Ritter, J.B., Miller, J.R., Enzel, Y. and Wells, S.G., 1995. Reconciling the roles of tectonism and climate in Quaternary alluvial fan evolution. Geology, 23(3), pp.245-248.

Scheinert, C., Wasklewicz, T. and Staley, D., 2012. Alluvial fan dynamics–revisiting the field. Geography Compass, 6(12), pp.752-775.

Schlitzer, R., 2024. Ocean data view. https://odv.awi.de

Schmidt, G., Franchi, F., Salvini, F., Selepeng, A.T., Luzzi, E., Schmidt, C. and Atekwana, E.A., 2023. Fault controlled geometries by inherited tectonic texture at the southern end of the East African Rift System in the Makgadikgadi Basin, northeastern Botswana. Tectonophysics, 846, p.229678.

Scholz, C.H., Koczynski, T.A. and Hutchins, D.G., 1976. Evidence for incipient rifting in southern Africa. Geophysical Journal International, 44(1), pp.135-144.

Shaw, P.A. and Thomas, D.G., 1992. Geomorphology, sedimentation, and tectonics in the Kalahari Rift. Israel journal of earth-sciences, 41(2-4), pp.87-94.

Shaw, P.A. and Thomas, D.S.G., 1988. Lake Caprivi: a late Quaternary link between the Zambezi and middle Kalahari drainage systems. Zeitschrift für Geomorphologie, pp.329-337.

Shaw, P.A., Bateman, M.D., Thomas, D.S. and Davies, F., 2003. Holocene fluctuations of Lake Ngami, Middle Kalahari: chronology and responses to climatic change. Quaternary International, 111(1), pp.23-35.

Shaw, P.A., Thomas, D.S. and Nash, D.J., 1992. Late Quaternary fluvial activity in the dry valleys (mekgacha) of the Middle and Southern Kalahari, southern Africa. Journal of Quaternary Science, 7(4), pp.273-281.

Stanistreet, I.G. and McCarthy, T.S., 1993. The Okavango Fan and the classification of subaerial fan systems. Sedimentary geology, 85(1-4), pp.115-133.

Stewart, B.A. and Jones, S.C., 2016. Africa from MIS 6-2: the florescence of modern humans. Africa from MIS 6-2: Population Dynamics and Paleoenvironments, pp.1-20.

Stock, J.D., 2013. Waters divided: a history of alluvial fan research and a view of its future. In: Shroder, J. (Editor in Chief), Wohl, E. (Ed.), Treatise on Geomorphology. Academic Press, San Diego, CA, vol. 9, Fluvial

Stokes, S., Haynes, G., Thomas, D.S.G., Horrocks, J.L., Higginson, M. and Malifa, M., 1998. Punctuated aridity in southern Africa during the last glacial cycle: the chronology of linear dune construction in the northeastern Kalahari. Palaeogeography, Palaeoclimatology, Palaeoecology, 137(3-4), pp.305-322.

Terrizzano, C.M., Morabito, E.G., Christl, M., Likerman, J., Tobal, J., Yamin, M. and Zech, R., 2017. Climatic and Tectonic forcing on alluvial fans in the Southern Central Andes. Quaternary science reviews, 172, pp.131-141.

Thomas, D. and Shaw, P.A., 1991. The Kalahari Environment. Cambridge University Press.

Thomas, D.S., O'Connor, P.W., Bateman, M.D., Shaw, P.A., Stokes, S. and Nash, D.J., 2000. Dune activity as a record of late Quaternary aridity in the Northern Kalahari: new evidence from northern Namibia interpreted in the context of regional arid and humid chronologies. Palaeogeography, Palaeoclimatology, Palaeoecology, 156(3-4), pp.243-259.

Vainer, S. and Ben Dor, Y., 2021. The Cosmolian program for simulating aeolian dynamics and its application to central Australia. Earth Surface Processes and Landforms, 46(9), pp.1631-1639.

Vainer, S., Dor, Y.B. and Matmon, A., 2018a. Coupling cosmogenic nuclides and luminescence dating into a unified accumulation model of aeolian landforms age and dynamics: The case study of the Kalahari Erg. Quaternary Geochronology, 48, pp.133-144.

Vainer, S., Erel, Y. and Matmon, A., 2018b. Provenance and depositional environments of Quaternary sediments in the southern Kalahari Basin. Chemical Geology, 476, pp.352-369.

Vainer, S., Matmon, A., Ben Dor, Y., Verrecchia, E.P., Eckardt, F. and ASTER Team, 2022. Eolian chronology reveals causal links between tectonics, climate, and erg generation. Nature Communications, 13(1), p.5714.

Vainer, S., Matmon, A., Erel, Y., Hidy, A.J., Crouvi, O., De Wit, M., Geller, Y. and ASTER Team, 2021. Landscape responses to intraplate deformation in the Kalahari constrained by sediment provenance and chronology in the Okavango Basin. Basin Research, 33(2), pp.1170-1193.

Vaks, A., Bar-Matthews, M., Matthews, A., Ayalon, A. and Frumkin, A., 2010. Middle-Late Quaternary paleoclimate of northern margins of the Saharan-Arabian Desert: reconstruction from speleothems of Negev Desert, Israel. Quaternary Science Reviews, 29(19-20), pp.2647-2662.

Vandenberghe, D., De Corte, F., Buylaert, J.P., Kučera, J., Van den haute, P., 2008. On the internal radioactivity in quartz. Radiation Measurements 43, 771-775.

Vezzoli, G., Garzanti, E., 2009. Tracking paleodrainage in Pleistocene foreland basins. The Journal of Geology, 117, 445-454.

Viseras, C., Calvache, M.L., Soria, J.M. and Fernández, J., 2003. Differential features of alluvial fans controlled by tectonic or eustatic accommodation space. Examples from the Betic Cordillera, Spain. Geomorphology, 50(1-3), pp.181-202.

Walker, T.R. and McKee, E.D., 1979. Red color in dune sand. United States Geological Survey Professional Papers, 1052, pp.61-81.

Wang, L., D'odorico, P., Ringrose, S., Coetzee, S. and Macko, S.A., 2007. Biogeochemistry of Kalahari sands. Journal of Arid Environments, 71(3), pp.259-279.

Warren, J.K., 2010. Evaporites through time: Tectonic, climatic and eustatic controls in marine and nonmarine deposits. Earth-Science Reviews, 98(3-4), pp.217-268.

Watchman, A.L. and Twidale, C.R., 2002. Relative and 'absolute' dating of land surfaces. Earth-Science Reviews, 58(1-2), pp.1-49.

Wilkinson, J., M., Miller, R., Eckardt, F., & Kreslavsky, M., 2023. Megafans of the Northern Kalahari Basin (Angola, Botswana, Namibia, Zambia). In J. Wilkinson & Y. Gunnell (Eds.), Fluvial Megafans on Earth and Mars (pp. 48-77). Cambridge: Cambridge University Press.

Wright, V., Canales, J.P., de'Enremont, N., Matende, K., Moffat, L., Giosan, L., Laletsang, K., Mapeo, R., Behn, M. and Ivory, S., 2021. Tectonostratigraphy of the northern Okavango Delta and Rift Zone, Botswana. Earth-ArXiv, https://doi.org/10.31223/X5W60J

Young, M.J., Gawthorpe, R.L. and Sharp, I.R., 2000. Sedimentology and sequence stratigraphy of a transfer zone coarse-grained delta, Miocene Suez Rift, Egypt. Sedimentology, 47(6), pp.1081-1104.

Yu, Y., Liu, K.H., Huang, Z., Zhao, D., Reed, C.A., Moidaki, M., Lei, J. and Gao, S.S., 2017. Mantle structure beneath the incipient Okavango rift zone in southern Africa. Geosphere, 13(1), pp.102-111.

Figure 1.

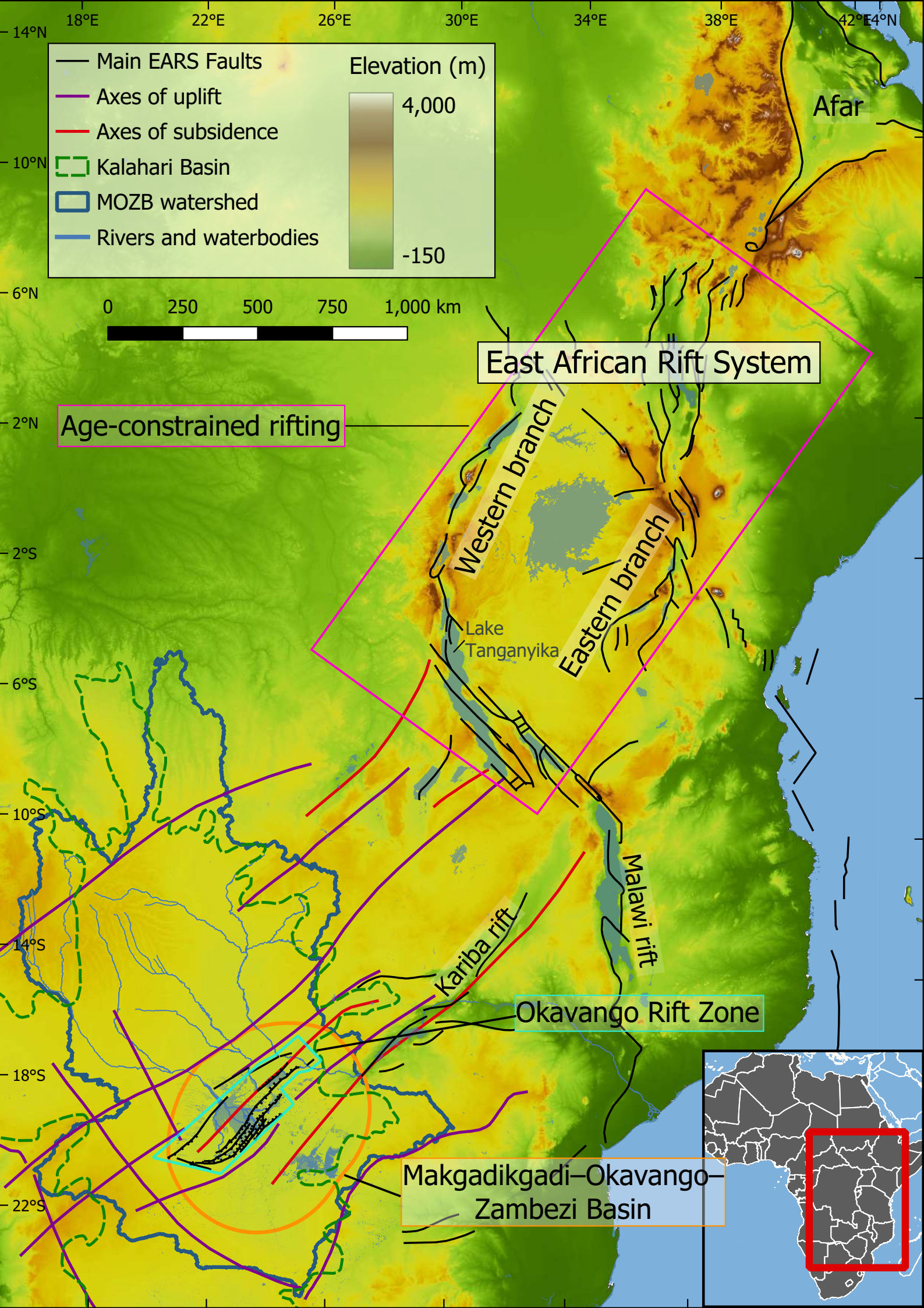
Main EARS Faults
Axes of uplift
Axes of subsidence
Kalahari Basin
MOZB watershed
Rivers and waterbodies
Elevation (m)
4,000
-150
0
250
500
750
1,000 km
18°E
22°E
26°E
30°E
34°E
38°E
42°E
14°N
10°N
6°N
2°N
2°S
6°S
10°S
14°S
18°S
22°S
Afar
East African Rift System
Age-constrained rifting
Western branch
Eastern branch
Lake Tanganyika
Malawi rift
Kariba rift
Okavango Rift Zone
Makgadikgadi–Okavango–Zambezi Basin

Figure 2.

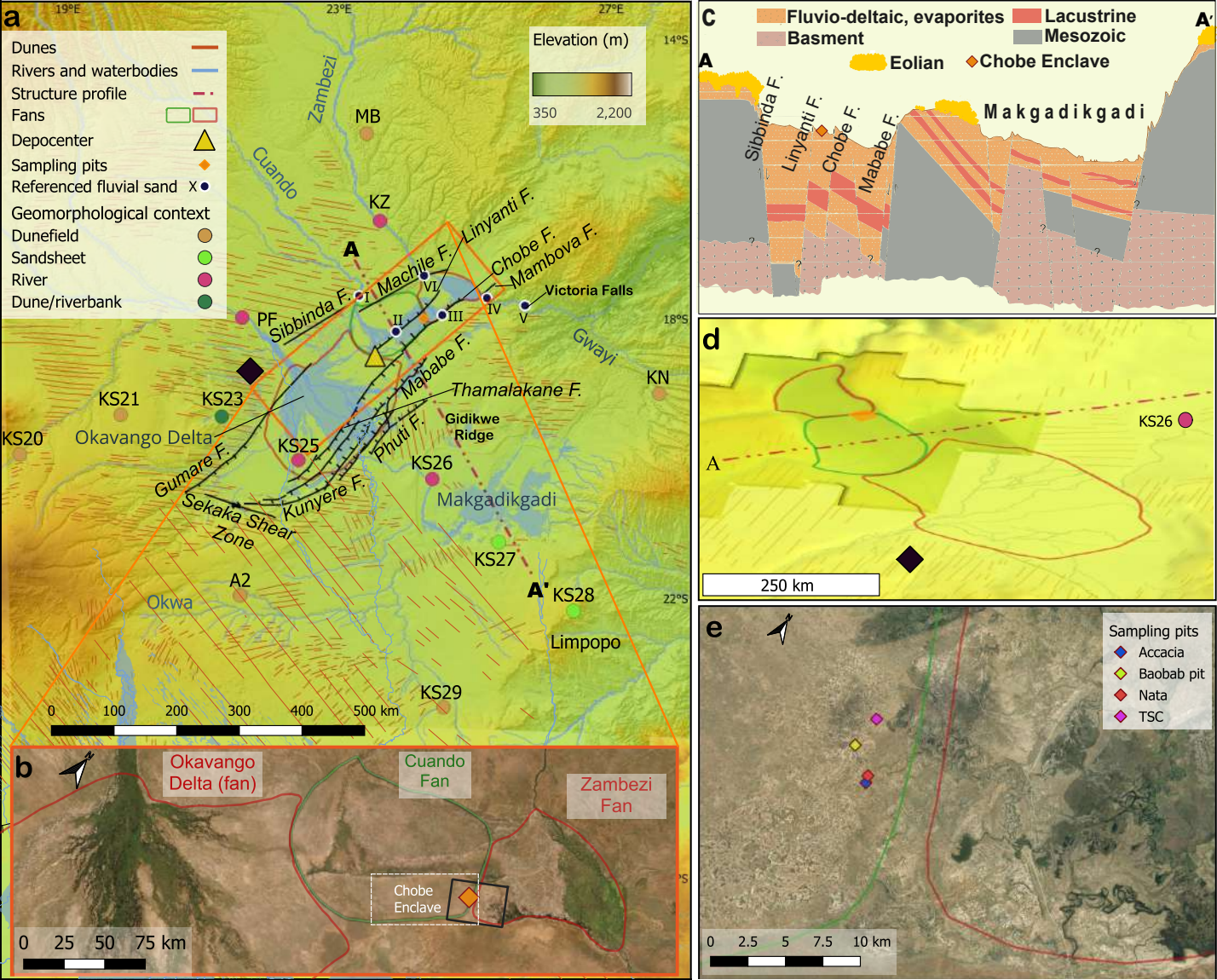
a
Dunes
Rivers and waterbodies
Structure profile
Fans
Depocenter
Sampling pits
Referenced fluvial sand
Geomorphological context
Dunefield
Sandsheet
River
Dune/riverbank
Elevation (m)
350
2,200
19°E
23°E
27°E
14°S
18°S
22°S
Zambezi
Cuando
Gwayi
Okwa
Limpopo
MB
KZ
PF
KN
KS20
KS21
KS23
KS25
KS26
KS27
KS28
KS29
A2
A
A'
Okavango Delta
Makgadikgadi
Sibbinda F.
Machile F.
Linyanti F.
Chobe F.
Mambova F.
Mababe F.
Thamalakane F.
Phuti F.
Gidikwe Ridge
Gumare F.
Kunyere F.
Sekaka Shear Zone
Victoria Falls
I
II
III
IV
V
VI
0
100
200
300
400
500 km
b
Okavango Delta (fan)
Cuando Fan
Zambezi Fan
Chobe Enclave
0
25
50
75 km
c
Fluvio-deltaic, evaporites
Basment
Lacustrine
Mesozoic
Eolian
Chobe Enclave
A
A'
Sibbinda F.
Linyanti F.
Chobe F.
Mababe F.
Makgadikgadi
d
KS26
A
250 km
e
Sampling pits
Accacia
Baobab pit
Nata
TSC
0
2.5
5
7.5
10 km

Figure 3.

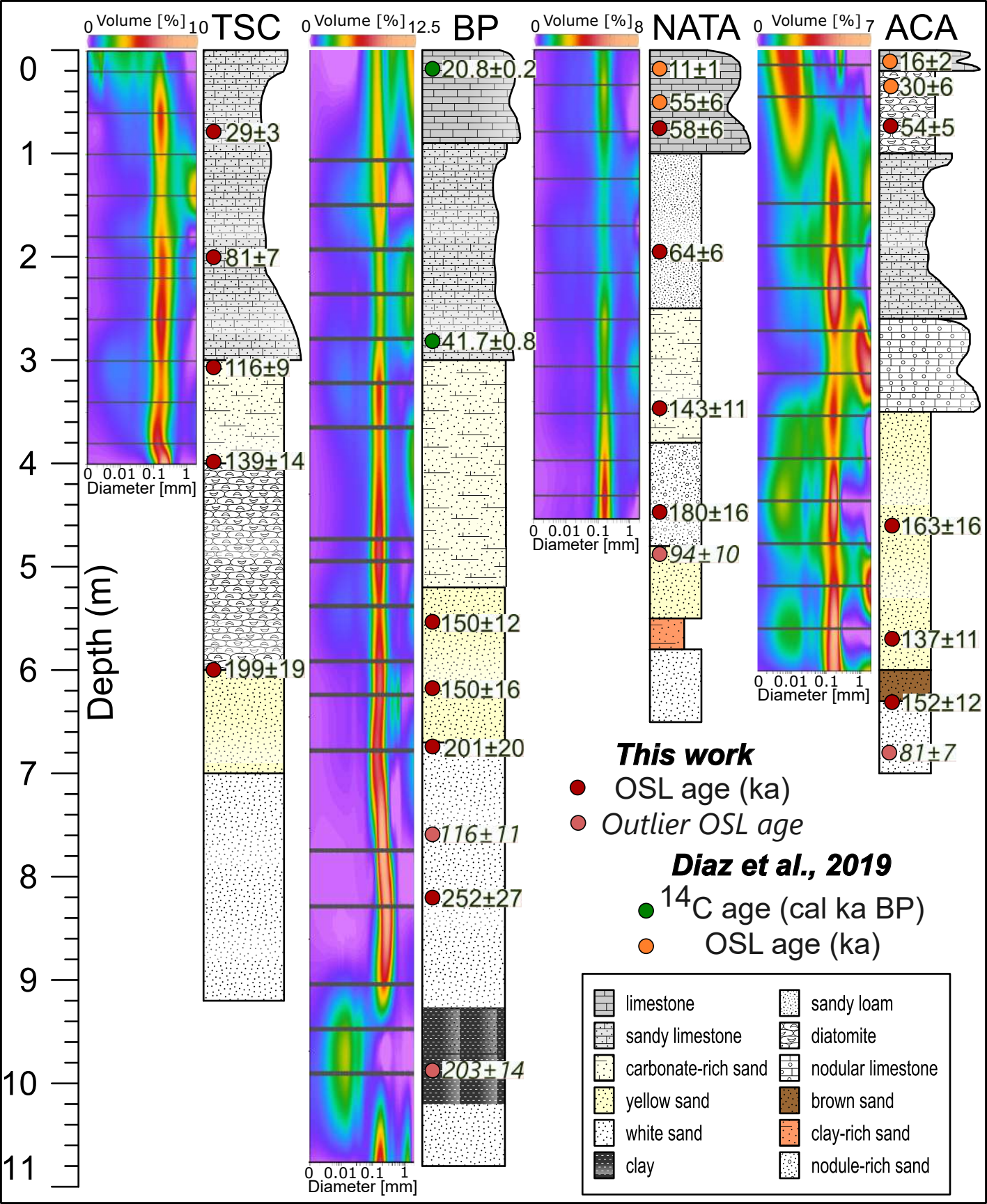
TSC
BP
NATA
ACA
Volume [%]
Diameter [mm]
Depth (m)
29±3
81±7
116±9
139±14
199±19
20.8±0.2
41.7±0.8
150±12
150±16
201±20
116±11
252±27
203±14
11±1
55±6
58±6
64±6
143±11
180±16
94±10
16±2
30±6
54±5
163±16
137±11
152±12
81±7
This work
OSL age (ka)
Outlier OSL age
Diaz et al., 2019
14C age (cal ka BP)
OSL age (ka)
limestone
sandy limestone
carbonate-rich sand
yellow sand
white sand
clay
sandy loam
diatomite
nodular limestone
brown sand
clay-rich sand
nodule-rich sand

Figure 4.

a

MOZB watershed
Axes of uplift
Axes of subsidence
MOZB depocenter
Elevation profile
Sand residence time (Myr)
0.91 - 1.05
1.14 - 1.59
2.17 - 2.22
Sampling pits
Graduated symbols
Distance from depocenter
CN points copy copy
Elevation

12°S
16°S
20°S
24°S
20°E
24°E
28°E
0 100 200 300 400 500 km

MB
KZ
KS20
KS21
KS23
KS25
KS26
KS27
KS28
KS29
KN
A2

b

1.43$^{+0.34}_{-0.25}$ A2
0.98$^{+0.26}_{-0.23}$ KZ
1.53$^{+0.32}_{-0.27}$ KN
2.22$^{+0.96}_{-0.69}$ MB
2.17$^{+1.02}_{-0.42}$ KS20
1.39$^{+1.48}_{-0.24}$ KS21
1.14$^{+0.39}_{-0.25}$ KS23
1.04$^{+0.24}_{-0.22}$ KS25
0.91$^{+0.24}_{-0.22}$ KS26
1.59$^{+0.8}_{-0.37}$ KS27
1.46$^{+0.35}_{-0.26}$ KS28
1.27$^{+0.81}_{-0.27}$ KS29

Residence time (Myr)

Erosion rate [m/Ma]
3 9 20
Displacement rate
eolian FLP
Overburden [m]
10 25
Correction
-fast 10% none

c

B B'
Elevation (m)
1300 1200 1100 1000 900
MB CE KS26 KS27 KS29
0 200 400 600 800 1000
Km

C C'
1800 1600 1400 1200 1000
KS20 KS21 KS23 KS25 CE KN
0 200 400 600 800 1000 1200 1400
Km

Figure 5.

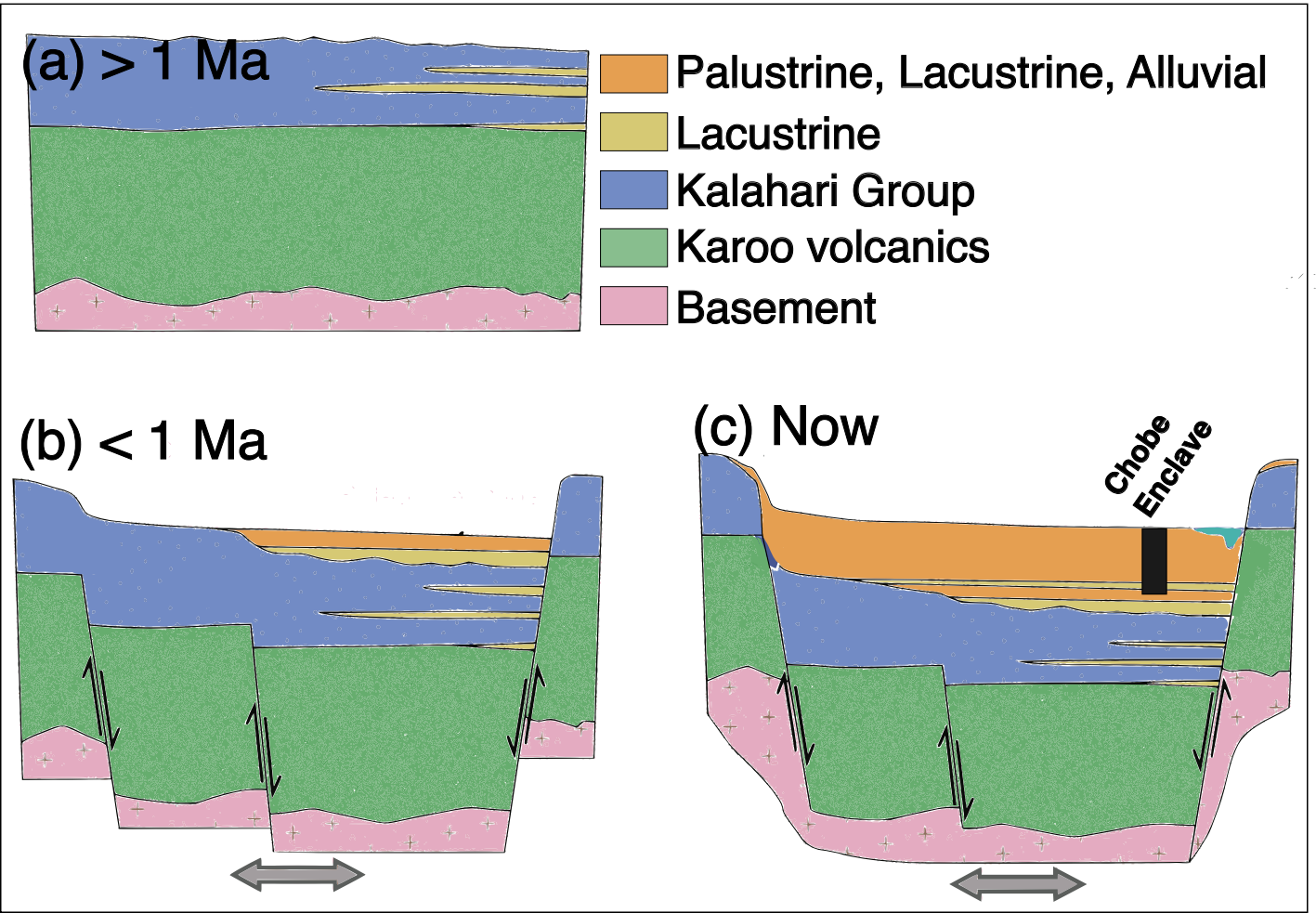
(a) > 1 Ma
Palustrine, Lacustrine, Alluvial
Lacustrine
Kalahari Group
Karoo volcanics
Basement
(b) < 1 Ma
(c) Now
Chobe
Enclave